



# NEEDS TAILORED **INTEROPERABLE** RAILWAY INFRASTRUCTURE

# NeTIRail

Needs Tailored Interoperable Railway Infrastructure

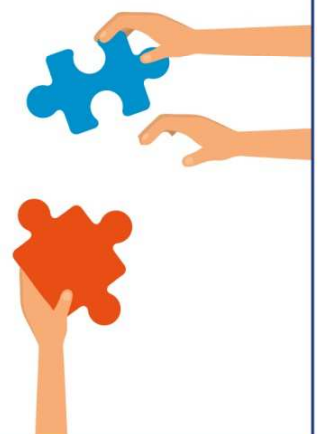
## Deliverable D2.6

**Tailoring track to avoid corrugations: Traffic dependant selection of rail cross-section, clips and pads to avoid or delay corrugation**

Submission date : 16 May 2018



*NeTIRail-INFRA is funded by the European Commission under the Horizon 2020 programme - Grant agreement n° 636237*



## Lead contractor

---

INTADER

## Contributors

---

SZ

USFD

UIC

## Project Coordinator

---

University of Sheffield, USFD

## Executive Summary

---

The deliverable D2.6 presents the research efforts of the NeTIRail-INFRA project in the understanding of the phenomenon of short pitch corrugation.

In the Section 1 of this deliverable, a three-dimensional (3D) finite element (FE) dynamic frictional rolling contact model is presented for the study of short pitch corrugation that considers direct and instantaneous coupling between the contact mechanics and the structural dynamics in a vehicle-track system. We examine the system responses in terms of vibration modes, contact forces and the resulting wear with smooth rail and corrugated rail with progressively increasing amplitude to infer the conditions for consistent corrugation initiation and growth. Wear is assumed to be the damage mechanism, and short pitch corrugation is modelled using wavelengths from field observations of a Dutch railway. The contribution of this Section is a global perspective of the consistency conditions that govern the evolution of short pitch corrugation. The main insights are as follows:

- 1) The longitudinal vibration modes are probably dominant for short pitch corrugation initiation.
- 2) During short pitch corrugation evolution, the interaction and consistency between longitudinal and vertical modes should determine the development of short pitch corrugation, and once a certain severity is reached, vertical modes become dominant.
- 3) In the case simulated, corrugation does not grow probably due to not only the different resulting main frequencies of the vertical and longitudinal contact forces, but also the inconsistency between the frequencies of the vertical and longitudinal vibration modes and the resulting wear. It is inferred that in the continuous process of initiation and growth of the corrugation, there should be a consistency between them, and this could be done by the control of certain track parameters.

Section 2 describes a catalogue of corrugations for the railway network in Turkey, including type of corrugation and a set of track parameters where the corrugation was located, including type of fastening system among other characteristics. In Section 3, the test conducted in Turkey to evaluate the responses of corrugation under different fastening systems is presented. Finally, in Sections 4 are the conclusions and recommendations.

### Contribution to the task T2.4, "life extension for plain line through preventing corrugation".

The main goal of T2.4 is to provide a better understanding of corrugation (rail surface irregularity and waviness) and what can be done to prevent it. One of the hypothesis in this task is that corrugation is influenced by the choice of fastenings and rail pads. In direction to prove the hypothesis, in this deliverable we present:

- A further analysis of the 3D FE modelling approach and new insights about short pitch corrugation. The global explanation of the dynamic conditions and the resulting corrugation damage are described. The results presented were published with acknowledgment to NeTIRail-INFRA in the journal Applied Sciences:

“S. Li, Z. Li, A. Núñez, and R. Dollevoet, “New insights into the short pitch corrugation development enigma based on 3D-FE dynamic vehicle-track coupled modelling in frictional rolling contact”. Applied Sciences, 2017 7(8), 807, Aug. 2017. DOI: 10.3390/app7080807.”

- Deviation from the grant agreement: the modelling approach is not able yet to develop corrugation from smooth rail condition. Thus, via the 3D-FE modelling approach was not possible to define links between certain clips and pads and corrugation. In view of this deviation, the experimental tests to be conducted in the Turkish railways include: 1) a catalogue of corrugation and track parameters, and 2) experiments on corrugated rail making use of the most usual clips and pads available from the industry.

## Table of contents

---

Executive Summary.....	3
Table of contents .....	5
Abbreviations and acronyms .....	7
1 New Insights into the Short Pitch Corrugation Enigma Based on 3D-FE Coupled Dynamic Vehicle-Track Modeling of Frictional Rolling Contact.....	8
1.1 Introduction .....	8
1.2 Model.....	12
1.2.1 FE Model .....	12
1.2.2 Corrugation Model.....	15
1.2.3 Validity of the Model .....	15
1.3 Contact Solutions at Corrugation.....	17
1.3.1 Normal Contact .....	17
1.3.2 Tangential Contact .....	20
1.4 Wear and Corrugation Simulation .....	21
1.4.1 Wear Model .....	21
1.4.2 Prediction of Major Field Observations .....	22
1.4.3 Analysis of Longitudinal and Vertical Rail Modes .....	23
1.4.4 Additional Comments .....	26
1.5 Relationship between Contact Forces and Wear as well as New Insights.....	26
1.5.1 Normal and Longitudinal Forces Do Not Exactly Follow Corrugation in Wavelength and Phase	27
1.5.2 Preferred Frequency of Contact Forces .....	28
1.5.3 Frequencies Converge to Develop Uniform Corrugation .....	29
1.5.4 Importance of the Proposed Modeling Approach and Track Parameters.....	30
1.5.5 Additional Discussions .....	31
1.6 References .....	32
2 Catalogue of Corrugation in Turkey.....	36
2.1 Brief summary about the corrugation catalogue.....	36
2.2 Examples of the corrugation catalogue .....	38

2.3	Conclusion and further recommendations.....	40
3	Test in Turkey.....	42
3.1	Brief introduction to test site.....	42
3.2	Selection of the test equipment and integration process .....	47
3.3	Methodology.....	55
3.4	Test results.....	55
3.4.1	For passenger trains.....	55
3.4.2	For freight trains .....	59
3.5	Discussion and conclusion .....	61
3.5	References .....	62
4	Conclusions .....	63
	Annex I : Corrugation Catalogue .....	65

## Abbreviations and acronyms

Abbreviation / Acronym	Description
3D-FE	Three-dimensional finite element
FE	Finite element
RCF	Rolling contact fatigue
UIC	Union of railway
P1	The falling edge of studied wave of corrugation
P2	The trough of studied wave of corrugation
P3	The rising edge of studied wave of corrugation
P4	The peak of studied wave of corrugation
ABA	Axle box acceleration
PSD	Power spectrum density
SZ	Slovenske Železnice – Slovenian Railways
TCDD	Türkiye Cumhuriyeti Devlet Demiryolları – Turkish IM
TUD	Delft University of Technology
USFD	The University of Sheffield
FFT	Fast Fourier Transform

# 1 New Insights into the Short Pitch Corrugation Enigma Based on 3D-FE Coupled Dynamic Vehicle-Track Modeling of Frictional Rolling Contact

---

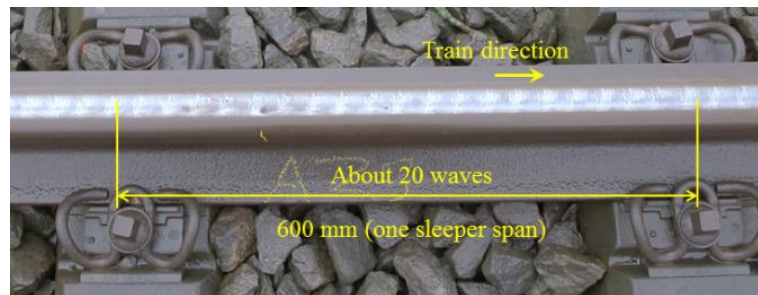
This chapter is based on the paper: S. Li, Z. Li, A. Núñez, and R. Dollevoet, “New insights into the short pitch corrugation development enigma based on 3D-FE dynamic vehicle-track coupled modelling in frictional rolling contact”. Applied Sciences, 2017 7(8), 807, Aug. 2017. DOI: 10.3390/app7080807

## 1.1 Introduction

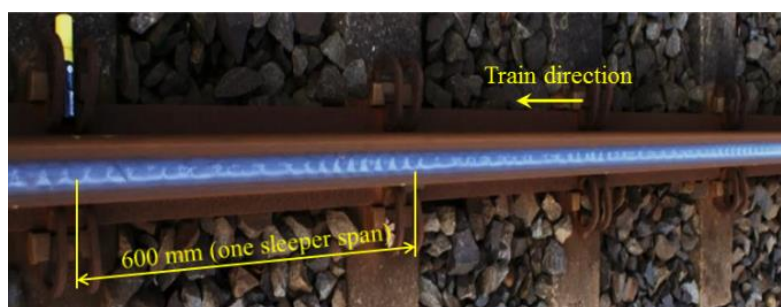
Rail corrugations are periodic defects commonly observed in all types of railway tracks. According to the current understanding of their development mechanisms, namely the damage mechanisms and wavelength-fixing mechanisms [1], rail corrugations can be classified into six groups: heavy haul, light rail, booted sleepers, contact fatigue, rutting and short pitch corrugation. Among these groups, the development mechanisms of short pitch corrugation (hereafter corrugation) are not fully understood. Although corrugation was identified more than a century ago and despite extensive research efforts [1,2], an effective solution has not been developed to avoid the corrugation problem, which remains an enigma that has puzzled many researchers and engineers [3,4]. Grinding appears to be the only effective corrective countermeasure; however, it increases maintenance costs and reduces the availability of the railway network. Thus, the development mechanisms of this phenomenon must be elucidated, and an effective solution for its control at an early stage must be identified.

Corrugation mainly occurs on straight tracks or gentle curves where contact does not occur between the wheel flange and rail gauge corner (Figure 1.1), and it usually manifests as shiny ripples and dark valleys. The typical wavelength is in the range of 20–80 mm, with amplitudes up to 100  $\mu\text{m}$  [1]. Corrugation is one of the most prominent problems for railway infrastructure managers because it increases the vibrations of the vehicle-track system and results in higher frequencies (more than 500 Hz) of the wheel-rail dynamic contact forces, which leads to accelerated degradation of vehicle-track system components and shortened service life [5]. In addition, the noise generated by vibrations is a nuisance to residents living near railway lines [1,6]. Because of the high level of noise, corrugation is also known as “roaring rail”. Corrugation can also generate rolling contact fatigue (RCF), such as squats [7] (Figure 1.1c).

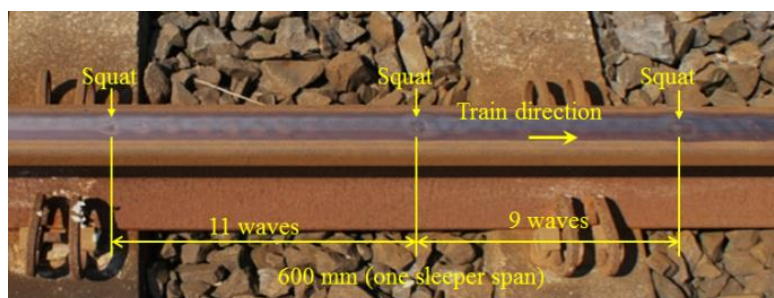




(a)



(b)



(c)

Figure 1.1 Short pitch corrugation and the resulting squats in the Dutch railway network. Wavelength and periodicity are distinguished (wavelength is the distance between two adjacent shining spots of ripples, and periodicity refers to the periodic pattern that contains multiple wavelengths of non-uniform amplitude of corrugation). (a) is at a gentle curve, and (b)-(c) are on straight tracks. (a) Uniform corrugation with a wavelength of approximately 30 mm. Squats have not yet developed, and a ballasted track with mono-block sleepers and fastenings with a W-shaped tension clamp is shown. Photo taken near Assen, the Netherlands. (b) Non-uniform corrugation of a constant periodicity of a sleeper span. The corrugation wavelength varies largely within a period. Squats have not yet developed, and a ballasted track with duo-block sleepers and fastenings with Deenik clips is shown. Photo taken near Steenwijk, the Netherlands. (c) Non-uniform corrugation with a periodicity shorter than a sleeper span. The corrugation wavelength is approximately 30 mm. The squats were caused by corrugation, and a ballasted track with duo-block sleepers and fastenings with Deenik clips is shown. Photo taken near Steenwijk, The Netherlands.

The main damage mechanism of corrugation is commonly considered to be wear caused by longitudinal wheel slip [8,9]. Plastic deformation is another possible damage mechanism [1], and it has been investigated by a numerical approach [10] and metallurgical analyses [11]. The wear and deformation underlying corrugation are differential, i.e., they are selective processes that “consistently” occur more at certain locations than at adjacent locations, which results in the accumulation and growth of typical wave patterns [12]. In this case, “consistently” indicates that the wear and deformation caused by one-wheel passage repeats the same wavelengths and phase angle of previous wheel passages, which results in the accumulation of wear and deformations and the initiation of corrugation growth. Because damage originates in the contact patch, the contact mechanics within the contact patch must be examined to better understand the damage mechanisms. Because dynamic wheel-rail contact is difficult to measure, a numerical analysis that can accurately simulate the vehicle-track dynamic interaction must be developed to analyze corrugation under controlled conditions [13].

The Hertzian treatment of the contact problem has usually been used to solve normal contact problems [9], whereas Kalker’s theories [14] are typically employed for the tangential direction [9]. The Hertzian solution considers that contact surfaces are frictionless smooth half-spaces. However, for worn or deformed profiles, such surface approximations may not hold in the vicinity of the contact patch [15,16]. Nielsen [16] employed a two-dimensional (2D) non-Hertzian contact model and found that the shape of the normal stress distribution was not elliptic because of the geometrical asymmetry. Correspondingly, the tangential stress distribution varies along different positions of the corrugation and may be responsible for the development of corrugation. In addition, the Hertzian theory and Kalker’s theory are based on statics. However, because the contact patch is on the order of 2 cm, which is similar to the corrugation wavelength, non-steady state processes caused by dynamic interactions must be considered [17,18].

In addition to long-term damage mechanisms, a short-term dynamic process is believed to fix the wavelength through structural dynamics [1,19]. The interaction between the short- and long-term mechanisms is represented by a feedback loop [1]. Three phenomena must be defined to understand corrugation development:

- (1) structural dynamics excitation caused by vehicle-track interactions,
- (2) loading response at the wheel-rail interface involving contact mechanics and
- (3) feedback from the contact and damage to the structural dynamics as determined by the direct coupling between the contact mechanics and structural dynamics.

In [9,20], a crucial understanding of the contact phenomena in the corrugation problem is provided. The model used in [9,20] solved the structural dynamics and contact mechanics problems separately in different models or steps.

In addition to a more elaborated treatment of the contact mechanics and an accurate representation of the vehicle-track interaction, we propose a combined modeling approach that includes the coupling and interplay of both the structural dynamics and contact mechanics problems. This solution is inspired by the work of Xie et al [9] and the question “why is roughness growth predicted by a simple contact model but not when complexity is increased to include non-Hertzian and non-steady contact conditions?”

The finite element method has been employed to investigate the development mechanism underlying squats in a vehicle-track system [7]. This modeling approach provides a good explanation for the development of corrugation initiated from isolated known railhead irregularities [21]. Because corrugation from isolated known railhead irregularities is of a short pitch type, this method could also be valid for investigating general types of short pitch corrugation. Corrugation that originates from railhead irregularities is caused by a dynamic force excited by known irregularities. In this case, the wavelength of the force is determined by the local track system, and the phase of the force is determined by the location of the irregularities. Thus, clear mechanisms of wavelength and phase fixing are involved. The wavelength and phase of the force at a given irregularity are always the same. Consequently, the resulting differential wear and/or plastic deformation is always in phase and damage accumulates under different wheel passages. In this way, corrugation can initiate and grow.

In the case of the general type of short pitch corrugation, a visually-identifiable initiation source is not observed. Although the wavelength might be fixed by the track structure, e.g., the “pin-pin” resonance [22] or the stick-slip process [23], the randomness of passing wheels and the track can lead to phase variations of the contact force so that the total effect of many wheel passages may cancel out or suppress the differential wear and deformation.

Regarding the latter situation, we must identify the causes of the dynamic forces that result in differential wear and differential plastic deformation, which remain in phase for the many different passing wheels such that the wear and deformation accumulate and corrugation can initiate and grow. Although the entire mechanism of the initiation and development of short pitch corrugation was not identified in this research, we present new insights based on numerical modeling that are consistent with field observations and can contribute to a better understanding of this enigma. We expect that the new insights provided here will trigger many new research efforts in the field that will ultimately produce a more complete understanding of the enigma and a final solution.

In this section, a 3D finite element (FE) approach is presented. This approach combines the vehicle-track interaction model of Li et al [7] with the solution for transient frictional rolling of Zhao et al [24]. The vehicle-track structural dynamics are directly coupled to the wheel-rail contact mechanics through the continuum treatment of the wheel and rail in the structure. The simulation of continuum mechanics has been reported to play “an important role in structural analysis” [25] and allows the instantaneous mutual influence of the contact mechanics and the structural mechanics to be simulated. This approach was presented in [26] to analyze the phase relationship between the given corrugation and the resulting periodic wear, and a similar approach was employed to study

corrugation in a high-speed railway [27]. In this chapter, the transient states of the rolling contact and wear are evaluated under a variety of loading conditions in relation to the dynamic forces excited by a passing wheel over a rail with and without corrugation. The damage mechanism is assumed to be limited to wear because the focus of this research is on the conditions that may lead to the consistent initiation and growth of corrugation. To account for plasticity, the method of Zhao [28] can be readily incorporated, which will be our future research focus.

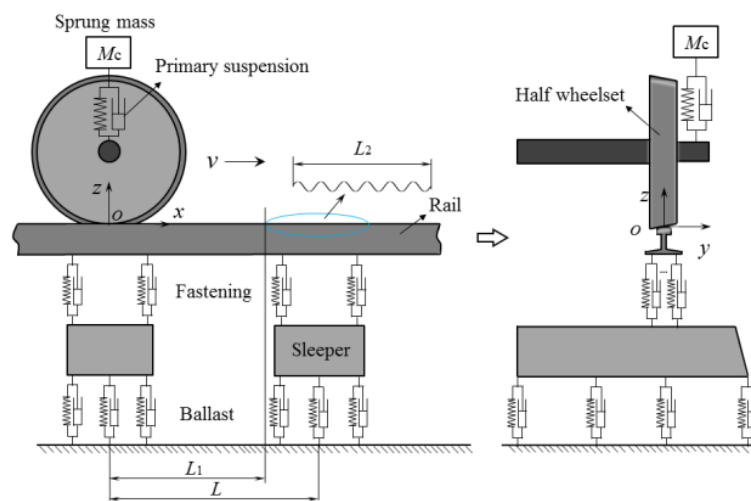
## 1.2 Model

### 1.2.1 FE Model

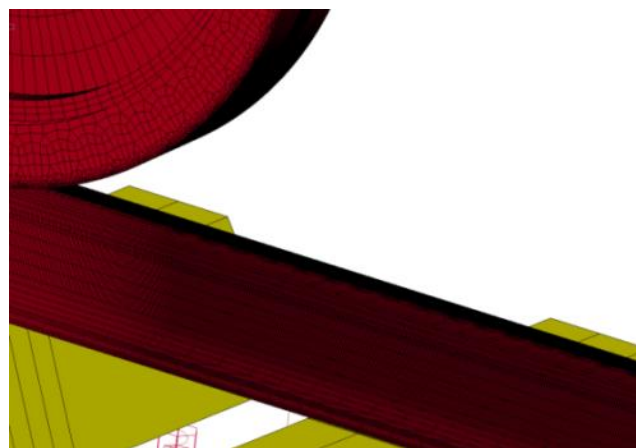
A schematic diagram of the 3D FE vehicle-track model is shown in Figure 1.2. The model is based on a symmetrical vehicle-track system assuming a straight track in which lateral movement is negligible. The wheel, rail and sleepers are modeled with solid elements. The nominal radius of the wheel is 0.46 m, and the tread coning is 1/40. The rail is a standard International Union of Railway (UIC) 54 profile with an inclination of 1/40. The contact surface of the wheel is smooth, whereas a length of corrugation is prescribed along the rail surface. The sprung mass (the weight of the car body and the bogie) is lumped into a mass element  $M_c$  supported by the primary suspension, which is represented by spring-damper elements. The sprung mass above a half wheelset is 1/8 of the sprung dynamic load of a whole vehicle, which is approximately a quarter of the sprung mass carried by a bogie. The fastening system and the ballast are also modeled as spring-damper elements. The track parameters are taken from [29] as shown in Table 1.1 and represent the typical Dutch railway system. In the FE model, the wheel and rail are meshed with 8-node solid elements. To achieve a solution of sufficient accuracy and an acceptable computation time, only the size of the elements in the solution zone is refined (0.8 mm  $\times$  0.8 mm in the longitudinal and lateral directions). The elements far from the solution zone are meshed at an element size up to 7.5 cm. These choices are based on [24], which concluded that the contact mechanics solution with an element size of 1.3 mm  $\times$  1.3 mm is sufficiently accurate when the FE approach used here is implemented for engineering applications. The total number of elements in the model is 1,135,384; the number of nodes is 1,297,900; and the model length is 18 m. In [30], a track length of 10 m was sufficient for problems of similar frequency and wavelength. The damage mechanism studied in this research is wear; thus, the wheel and rail materials are assumed to be elastic. A Coulomb friction law is employed with a friction coefficient  $f_c$  of 0.6 as in [31]. In the literature, the friction coefficient of dry wheel-rail contact is reported to be between 0.4 and 0.65 [32].

The solution process of the simulation includes two steps: an implicit analysis (using Ansys) and an explicit analysis (using Ls-dyna). The implicit analysis is performed to identify the initial deformation in the equilibrium position of the vehicle-track system. Then, the wheel is set to roll along the rail with a constant speed  $v = 38.9$  m/s (corresponding to the typical Dutch passenger train speed of 140 km/h). An explicit integration scheme with a central difference method is then implemented to solve the wheel-rail frictional rolling contact problems. The displacements obtained from the implicit process

are used as the initial state of the explicit integration process. If the time step ( $4.67 \times 10^{-8}$  s in this model) is smaller than the critical time step ( $5 \times 10^{-8}$  s) determined by the Courant criterion [33], convergence is guaranteed. By keeping the time step sufficiently small, the model can include all necessary vibration modes. In the explicit analysis, the frictional rolling is modeled using a surface-to-surface algorithm with the penalty method described in [34]. Because of the nature of explicit integration, the effect of transient rolling and the high-frequency dynamic behavior of the vehicle-track system excited by the moving wheel are automatically included in the solution.



(a)



(b)

Figure 1.2 Vehicle-track frictional rolling model in 3D. (a) Schematic diagram of the model. (b) FE model in 3D.

**Table 1.1 Vehicle parameters and track parameters**

Parameters		Values		Parameters		Values	
Wheel load		116.8 kN		Young's modulus		210 GPa	
Primary suspension	Stiffness	1.15 MN/m	Wheel and rail material	Poisson's ratio	0.3		
	Damping	2.5 kNs/m		Density	7800 kg/m <sup>3</sup>		
Rail pad	Stiffness	1300 MN/m	Sleeper	Young's modulus	38.4 GPa		
	Damping	45 kNs/m		Poisson's ratio	0.2		
Ballast	Stiffness	45 MN/m		Mass density	2520 kg/m <sup>3</sup>		
	Damping	32 kNs/m		Spacing ( <i>L</i> )	0.6 m		

As shown in Figure 1.2a, a distance  $L_1$  is used during the explicit process to diminish the effect of vibration excited by imperfect initial equilibrium because of numerical errors from the implicit solution. A total of 10 waves of corrugation with length  $L_2$  are introduced after  $L_1$ . The traction coefficient  $\mu$  is defined as follows:

$$\mu = F_L / F_N \leq f_c \quad (1)$$

where  $F_N$  is the normal contact force and  $F_L$  is the resultant tangential (creep) force in the longitudinal direction caused by an applied torque. Different traction coefficients produce different adhesion-slip states, as well as damages. In the subsequent analysis, a traction load corresponding to 40% of the static normal contact force is applied via a torque about the axis of the wheel. This produces a  $\mu$  of 0.4, which is usually the maximal traction coefficient of rolling stock [35,36]. Because of the dynamic nature of vehicle-track interactions, especially in the presence of corrugation, the actual contact forces are not constant. Therefore, the instantaneous traction coefficient varies with time and space along the track, and the actual value of the traction coefficient deviates from the static value. Regarding creepage, the approach of [7,24] is used in this research, where a constant driving torque is specified. The resulting creepage fluctuates with the corrugation [27].

A few additional remarks on the model are warranted. Note that high friction and traction coefficients are used. In [37,38], high traction was reported to facilitate corrugation development. Additionally, regarding the traction coefficient, we assume that the damage mechanism is wear. Hence, a large value is chosen to ensure a high longitudinal contact force and thus obtain high wear. A large traction coefficient indicates a large slip zone. A large slip zone aids in the visualization of changes in the contact patch caused by corrugation; thus, it is easier to visualize and compare the contact solutions [24]. Finally, the model does not include brake disks or gears and will not represent torsional vibrations. Torsional wheelset vibrations have been considered as a cause of corrugation at curves [1,39,40]; however, recent research [41] has shown that torsional wheelset vibrations are not correlated with corrugation development at curves. Torsional vibration is also considered in [42] for corrugation related to vibration up to about 100 Hz. In this research, the frequencies considered are up to 2000 Hz.

### 1.2.2 Corrugation Model

In this section, corrugation with a sinusoidal profile is used as a test case. This choice is based on field observations, such as those shown in Figure 1.1a. Moreover, our work is a continuation of previous research in which corrugation was assumed to have a sinusoidal profile [3,9,43–46]. A sinusoidal corrugation with a constant wavelength is applied to the rail surface expressed by the equation:

$$z(x) = A \cos\left(\frac{2\pi x}{\lambda} + \theta\right) - A \quad (2)$$

where  $A$  is the amplitude of the corrugation,  $\lambda$  is the wavelength and  $\theta$  is the phase. The second term  $-A$  guarantees that the peak of the corrugation is not higher than the initial profile of the rail surface.

The wavelength is 30 mm, which is approximately equal to one of the recorded corrugation wavelengths on the Dutch railway network shown in Figure 1.1a,c (see the measurement in Figure 1.3a). For the analysis, 10 waves are considered; thus,  $L_2$  equals 300 mm. The corrugation considered is located above a sleeper support (as shown in Figure 1.1b), which has been reported as a position where corrugation is more likely to develop [22]. To examine the wheel-rail contact during the growth process of the corrugation, the amplitudes of  $A = 0 \mu\text{m}$  for smooth rail and  $A = 2.5 \mu\text{m}$ ,  $5 \mu\text{m}$ ,  $10 \mu\text{m}$  and  $20 \mu\text{m}$  for corrugated rail are modeled (the peak-to-trough distance is twice the amplitude). By maintaining  $\theta$  between  $-\pi/2$  and  $\pi$ , contact solutions can be studied at different locations within one complete corrugation wavelength, i.e., the falling edge (P1), the trough (P2), the rising edge (P3) and the peak (P4), as shown in Figure 1.3b. Figure 1.3c shows a magnified 3D configuration of the corrugation in the rail surface.

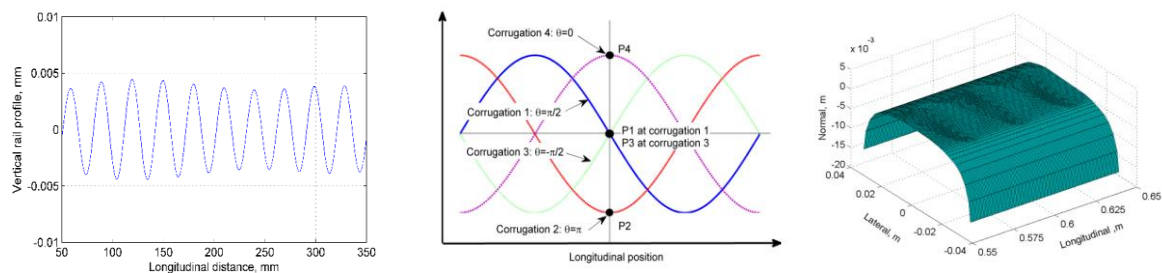


**Figure 1.3 Modeled corrugation: (a) field measurement of corrugation (27–33 mm bandpass filtering); (b) schematic diagram of the corrugation and 4 positions (blue line: P1, red line: P2, green line: P3 and magenta line: P4); and (c) illustration of the applied corrugation (Corrugation 2 with P2 at 0.6 m) in the rail surface with 5× magnification (only 3 complete waves are plotted).**

### 1.2.3 Validity of the Model

To characterize the dynamics in the frequency range of interest as discussed in the Introduction, corrugation modeling should consider the following issues: static and dynamic contact problems

should be validated; structural dynamics should be considered [47]; and coupling between the contact problem and structural dynamics should be validated.

With respect to the contact problems, a method similar to that of [24] is used herein. This method is suitable for resolving dynamic contact problems, and its validity has been demonstrated by the close reproduction of the evolution of squats [7,48]. Moreover, this method has been verified as suitable for resolving static contact problems based on the established solutions of Hertz, Spence, Cataneo, Mindlin and Kalker [24,49].

To validate the structural dynamics, (a) the approach used in this research can reproduce the hammer test [50]; thus, the model can simulate measured track receptance based on identified track parameters. (b) Furthermore, the model can simulate axle-box acceleration (ABA) measurements [30,51]. Consequently, the model can capture the dynamics of wheels and tracks and the interaction between the vehicle and the track in the relevant frequency range.

With respect to assessing the validity of the model for a vehicle-track system with direct coupling between the contact problem and structural dynamics, the model exhibits a good representation of the dynamic response (spatial and frequency) of corrugation induced by squats. As noted in [21], “the model provides a good explanation for the development of corrugation initiated from isolated railhead irregularities”. Thus, in this research, the challenge is to extend the model to the study of the more general type of corrugation that does not present clear local irregularities as the source of corrugation initiation.

As will be discussed in greater detail in Section 1.4.2 on the prediction of major field observations, the simulated wear in Figure 1.8a is in agreement with the field observations shown in Figure 1.1b,c. Here, the irregular distribution of wear along one sleeper span is clear, and the observations and simulation are in agreement. In the chapter, other agreements between the model results and field observations are discussed in greater detail later in the text. For example, the contact solutions that indicate that wear is the more probable damage mechanism at the corrugation trough [1,11,52] will be described in Section 1.3, and the occurrence of squats in agreement with the observation in Figure 1.1c will be explained in Section 1.4.2. These summaries comprehensively describe and analyze how the model was validated.

For other track and vehicle field data, typical parameters of the Dutch railway are used [29]. For modeling corrugation, a sinusoidal profile is employed based on field measurements (Figure 1.3a) and observations (Figure 1.1a).



## 1.3 Contact Solutions at Corrugation

### 1.3.1 Normal Contact

The FE approach defines whether a node is within the contact patch through the node force. A node is in contact if:

$$|F_{n,N}| > 0 \quad (3)$$

where  $F_{n,N}$  is the nodal force in the direction normal to the local surface. Because of the presence of corrugation, the stress and slip distributions will vary along a corrugation wavelength. Those differential distributions of the normal pressure, shear stress and slip are the direct factors in corrugation development.

Figure 1.4a shows the changes in the contact patch size at P1, P2, P3 and P4 with increasing amplitude  $A$ . Compared with  $A = 0 \mu\text{m}$ , an increase in size of up to 16% at P2 is observed in the case of  $A = 20 \mu\text{m}$ , and the increase is approximately 4% at P3. At the other two positions, the changes are minor. The maximum contact patch size is approximately  $200 \text{ mm}^2$  ( $A = 20 \mu\text{m}$ ) at P2, i.e., the corrugation trough, whereas it is approximately  $170 \text{ mm}^2$  when the rail is smooth. Figure 1.4b displays the maximum contact pressure along the longitudinal axis ( $y = 0 \text{ mm}$ ) for different corrugation amplitudes  $A$ . As the corrugation amplitude increases from  $0$ – $20 \mu\text{m}$ , the contact pressure at P2 drops significantly to 56% of the original level, i.e., from  $1320$ – $745 \text{ MPa}$ . This decrease is partly because of the 15% increase in the contact patch size (Figure 1.4a). At P1 and P3, the maximum pressure declines slightly to 78% of the original level. An increase in pressure of 6% is observed at P4 for the case of  $A = 20 \mu\text{m}$ .

Figure 1.5 shows a typical profile of the variation of the magnitude of normal force, contact size and maximum contact pressure along the longitudinal axis. In the figure, the typical normal force is the lowest at trough P2 and the highest at peak P4, with intermediate values at points P1 and P3. As the corrugation amplitude increases, the normal contact force at P2 decreases and the area of the contact patch increases; thus, the pressure decreases. At P4, the normal contact force increases, and the area of the contact patch decreases; thus, the pressure increases. At P1 and P3, the normal contact force and the area of the contact patch are intermediate between cases P2 and P4. These patterns are further evident in Figure 1.4b, where the maximum contact pressure of P1 and P3 for the different corrugation amplitudes decreases, although it does not decrease as strongly as in the case of P2.

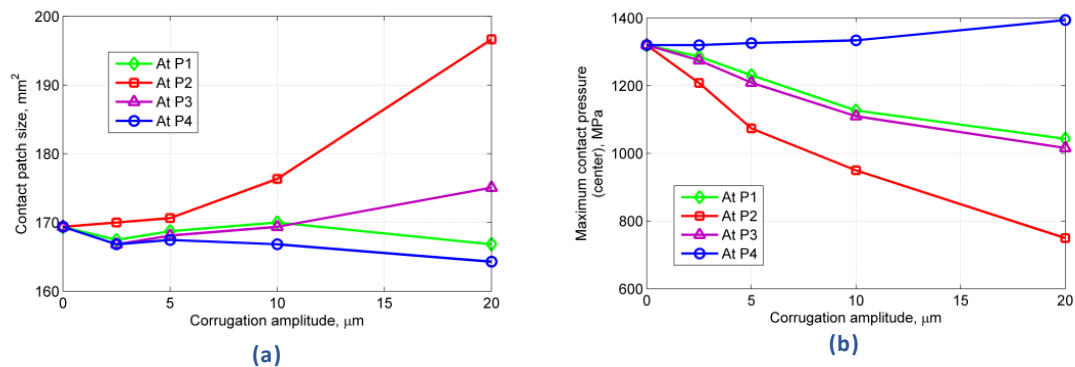


Figure 1.4. Influence of corrugation amplitude on the size of the contact patch and the maximum contact pressure along the longitudinal axis  $y = 0$  mm. (a) Contact size; (b) contact pressure.

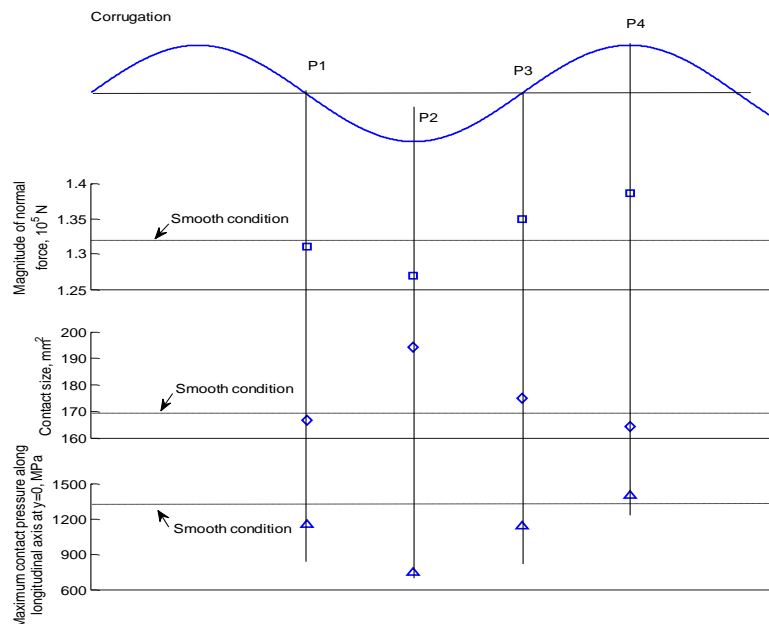


Figure 1.5. Magnitude of the normal force contact size and maximum pressure along the longitudinal axis at ( $y = 0$  mm) at the four analyzed positions P1, P2, P3 and P4 ( $A = 20 \mu\text{m}$ ).

Figure 1.6 shows the projections of contact pressure and shear stress onto the  $xOy$  plane, the shape of the contact patch under the smooth condition and the evolution within one corrugation wavelength from P1 to P4 when  $A = 20 \mu\text{m}$ . Most shapes are not elliptic and thus differ from the Hertzian solution. Because of the downhill slope of the corrugation at P1, a large drop in pressure is observed at the leading edge of the contact patch and vice versa at P3. Thus, the pressure distributions at P1 and P3 take the shapes of a “waning crescent moon” and “waxing crescent moon”, respectively. At P2, the maximal pressure shifts to the field and gauge sides, thereby decreasing the contact pressure in the contact patch center to 600–800 MPa. The pressure distribution at P4 is close to the solution under

the smooth rail except for a slight shrinkage of the contact patch at the leading and trailing edge centers. The maximum pressure is slightly higher than that at the other locations as shown in the pressure scaling color bar.

As also shown in Figure 1.5, the pressure variation within a corrugation wavelength along the longitudinal axis  $y = 0$  mm is approximately in phase with the corrugation. Furthermore, the shapes of the contact patch differ from those under the smooth rail condition. Part of the contact patch is not present in the leading area at P1, in the trailing area at P3 and in both the leading and trailing areas at P2 and P4. Thus, the deviation from a Hertzian solution is large and further exacerbated by increases in the corrugation amplitude.

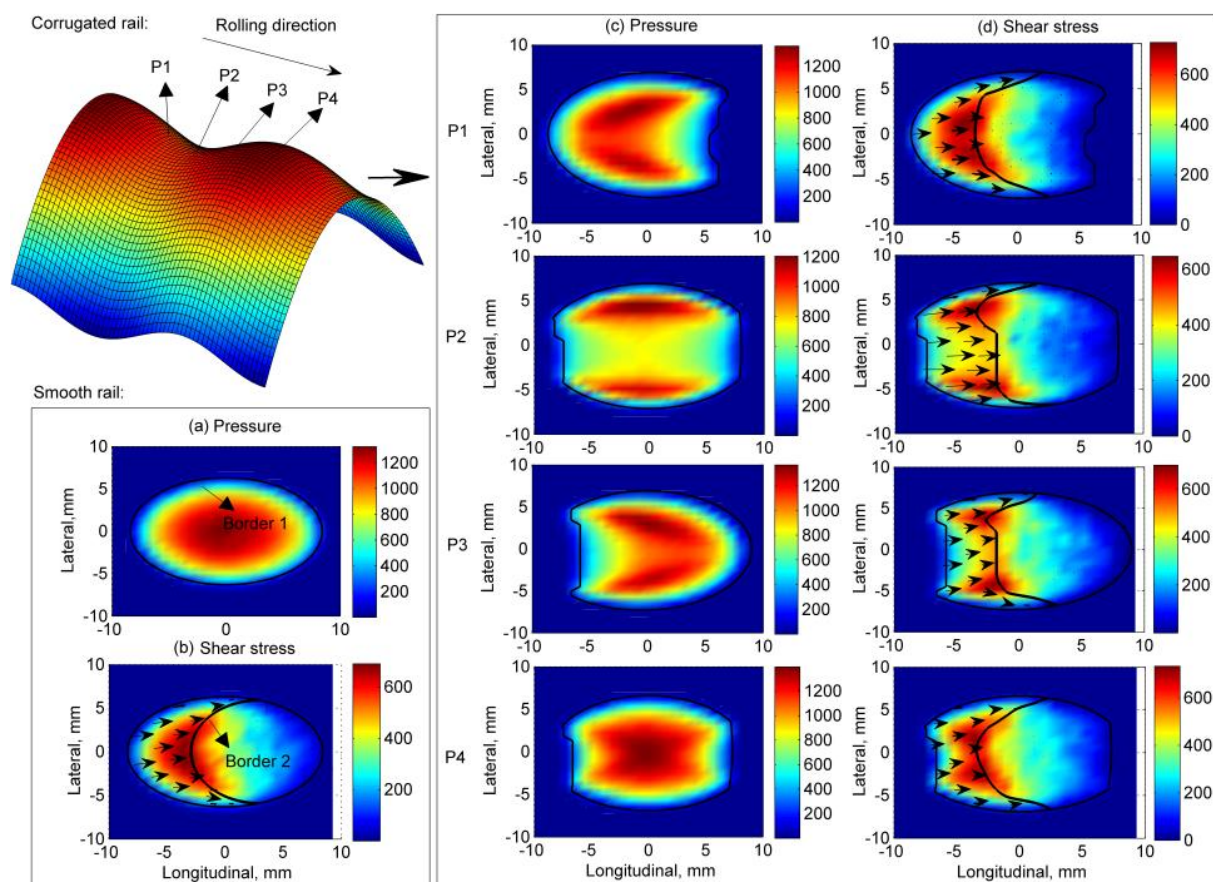


Figure 1.6. Contact pressure, shear stress, contact patch, adhesion-slip distributions and vector graphs of micro-slips (vectors in Figure 1.6b,6d) when  $A = 20 \mu\text{m}$  along one corrugation wavelength (P1–P4) (projection onto the xOy plane; Border 1: contact patch border; Border 2: adhesion-slip distribution border).

### 1.3.2 Tangential Contact

Figure 1.6b,d show the surface shear stress distributions when the rail is smooth and corrugated, respectively. In the presence of corrugation, especially when the amplitude is large, e.g.,  $A = 20 \mu\text{m}$ , the distributions of the shear stress differ from those of the smooth rail case. Similar to the pressure distributions, the maximum shear stress, which occurs in the central part and at the adhesion-slip boundary within the contact patch, is cut in the middle and protrudes on the gauge and field sides, especially at P2 and P3. The development of the surface shear stress with the increase in corrugation amplitude follows a trend similar to that of the normal pressure in the slip zone of the contact patch.

When a tangential force is applied, slip arises in the contact area. In the adhesion zone, there should not be relative slip between the contacting particles of the wheel and rail where the wheel and rail surfaces stick together. There should, however, be relative slip between the contacting particles of the wheel and rail surfaces in the slip zone. The tangential contact force  $F_{n,T}$  at a node in the slip zone equals the bound of the tangential nodal force, which is the product of the nodal force  $F_{n,N}$  in the normal direction and the friction coefficient  $f_C$  according to Coulomb's law. In the adhesion zone, the tangential nodal contact force is lower than the bound. Therefore, a node is in a slip zone if:

$$f_C |F_{n,N}| - |F_{n,T}| < \varepsilon_T \quad (4)$$

where  $\varepsilon_T$  is the tolerance. In this case,  $\varepsilon_T$  is 5% of the maximal tangential nodal force in the contact patch.

The adhesion-slip distribution in the presence of corrugation is shown in Figure 1.6d. The boundary between the adhesion and the slip zones at P2 and P3 is far from elliptic [14]. As assumed, differential wear proportional to the frictional work [9,18,22] causes the development of corrugation. Frictional work only occurs in the slip zone. Therefore, the size of the slip zone in the contact patch, as well as the magnitude of the slip might be indicators of corrugation development.

In Figure 1.7a, changes in the size of the slip zone with increases in corrugation amplitude at P1, P2, P3 and P4 are shown. The size fluctuates slightly at  $A = 0-10 \mu\text{m}$ . To study the trend of change, the corrugation amplitude is further extended to  $30 \mu\text{m}$ . When the rail is smooth, the size of the slip zone is approximately  $69 \text{ mm}^2$ , which is 40% of the whole contact patch ( $170 \text{ mm}^2$ ). After the initial fluctuations at  $A = 2.5 \mu\text{m}$  and  $5 \mu\text{m}$ , the value at P2 presents the largest change and increases up to  $98 \text{ mm}^2$  at  $A = 30 \mu\text{m}$ , which is 57% of the total smooth contact zone. At the other three positions, the change in the slip zone size is small. Specifically, at P3, this value remains almost at the same level, whereas at P1 and P4, a 10% decrease is observed compared with that of the smooth rail ( $A = 30 \mu\text{m}$ ).

Figure 1.7b shows the change in the slip distribution along the longitudinal axis  $y = 0 \text{ mm}$ . The maximum slip at P2 is much larger than that of the other cases, which is in agreement with the trend shown in Figure 1.7a. At P3 and P4, the magnitudes of the slip decrease compared with that of the smooth rail. The increase in the size of the slip zone and the maximum magnitude of the slip at P2 may

indicate that large micro-slips in the trough could be a major driver of corrugation development. The distribution of the slip within the contact patch is shown in Figure 1.6b,d.

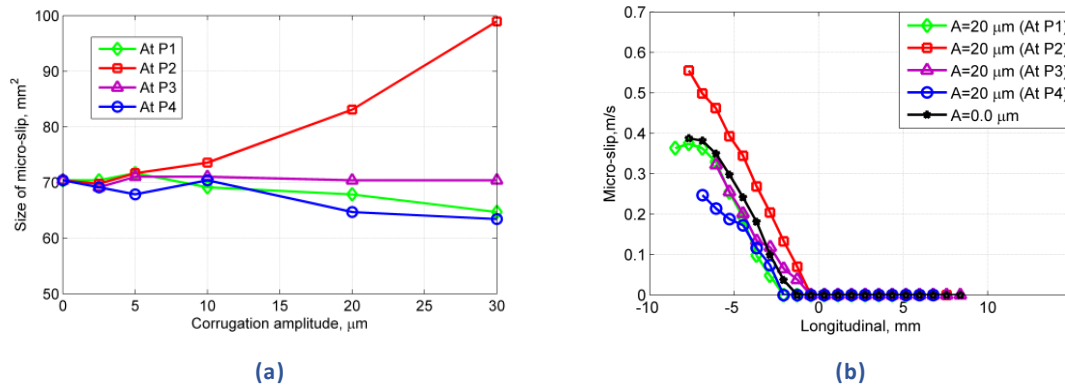


Figure 1.7. Size of the slip zone as a function of the corrugation amplitude and slip distribution along the longitudinal axis  $y = 0$  mm at the four positions. (a) Size of slip zone; (b) slip along the longitudinal axis  $y = 0$  mm.

## 1.4 Wear and Corrugation Simulation

### 1.4.1 Wear Model

The contact solutions in the presence of corrugation (as previously discussed) are used to calculate the frictional work, which is considered proportional to wear [9,18,22]. This section examines whether corrugation will grow under the given conditions by comparing the phases of wear and corrugation. To consider a whole sleeper, the applied corrugation of length  $L_2$  in Figure 1.2a is extended along the rail to start at  $x = 0.87$  m to cover both the middle sleeper span and sleeper support. The frictional work is calculated in the contact patch for each element for a whole wheel passage, i.e., from element entry until leaving contact. The wear of an element is as follows:

$$w(x, y) = kW_f(x, y) = k \sum_{i=1}^N \tau_i(x, y) v_i(x, y) \Delta t \quad (5)$$

where  $k$  is the wear coefficient,  $W_f(x, y)$  is the frictional work,  $\tau_i(x, y)$  and  $v_i(x, y)$  are the local tangential stress and slip, respectively, and  $N$  is the number of time steps  $\Delta t$  during which the element passes through the contact patch. The wear coefficient  $k$  is a constant that depends on the material, lubrication and temperature among other factors [8,9,53–55]. In this work, the calculated wear is normalized with respect to the average value of the wear under the smooth rail condition. This normalization is performed because the phase angle between wear and corrugation determines whether the corrugation will grow, which represents our main concern and is not directly affected by

the wear coefficients. It is part of further research to include measurements of the wear coefficients to guide maintenance.

#### 1.4.2 Prediction of Major Field Observations

In reality, the rolling of the wheel along the rail excites a range of vibrations of the structure and continua in the system. However, only a few of the vibration components are directly related to the corrugation. The corrugation wavelength observed in the field and introduced in the model is 30 mm, and the wavelength of short pitch corrugation is typically 20–80 mm, while the calculated wear is high-pass filtered to remove wear patterns shorter than 20 mm.

The wear along the longitudinal axis  $y = 0$  mm is studied. Figure 1.8a (which mentioned in Section 1.2.3) shows the distribution of the simulated wear along the rail with different corrugation amplitudes for the P4 corrugation position of  $\theta = 0$ , with 1.2 m as the corrugation peak. The results for the other corrugation positions show similar trends and are not presented. The wear is not uniform along the rail; thus, corrugation development will not be uniform under the evaluated conditions. Comparing the field observations in Figure 1.1 with the wear simulation results in Figure 1.8a reveals that the model closely reproduces the conditions in Figure 1.1b,c in terms of predicting the periodicity of the wear and the number of corrugation waves in the periodicity. The periodicity in Figure 1.1c is nine and 11 waves. The periodicity in Figure 1.8a is nine waves between the largest peak-to-trough wear magnitudes at 0.96 m and 1.23 m. In Figure 1.1c, the periodicity is counted between the squats because the squats should have been caused by the most severe corrugation, i.e., the largest wear.

Furthermore, the results agree well with the field observations (Figure 1.1). Specifically, the model predicts that the largest wear occurs at 1.23 m above a sleeper centered at 1.2 m (Figure 1.8a). This is in agreement with Figure 1.1c, in which one of the squats was above a sleeper, and with those in Figure 1.1b, where the corrugation was always the most severe above the sleepers. Rails above sleepers have been reported to be more prone to corrugation [22]. The inset in Figure 1.8a shows that the magnitude of wear decreases as the corrugation amplitude increases. This pattern can be understood in relation to Figures 1.6 and 1.7b because the wear is proportional to the product of the shear stress and the slip. The slip at  $A = 20 \mu\text{m}$  in Figure 1.7b is generally equal to or less than that at  $A = 0 \mu\text{m}$ , except at P2. The shear stress at  $A = 20 \mu\text{m}$  in Figure 1.6 is always less than that at  $A = 0 \mu\text{m}$ , and the difference is large for P2 and P3.

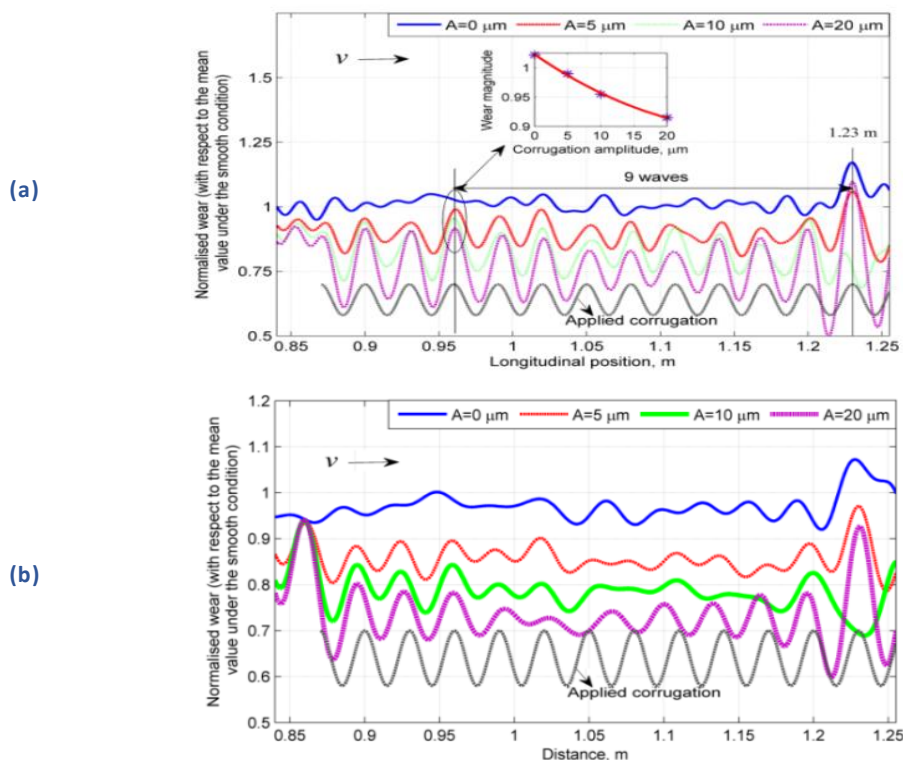


**Figure 1.8. Distribution of wear at different corrugation amplitudes obtained for the corrugation in Figure 1.3b with  $\theta = 0$  and P4 at 1.2 m. The middle of a sleeper is at 1.2 m, and the midpoint between two sleepers is at 0.9 m. (a) High-pass filtered at  $\lambda = 20$  mm. (b) High-pass filtered at  $\lambda = 30$  mm.**

The wear in Figure 1.8a is of the same wavelength and phase as the modeled corrugation. Thus, the existing corrugation will be erased by wear and will not grow, and if the rail is smooth, no corrugation will initiate. This finding is reasonable because the simulation is based on nominal track parameters; in reality, many tracks are indeed free of corrugation. Thus, the results indicate that corrugation is sensitive to the system parameters, e.g., rail fastening [41].

### 1.4.3 Analysis of Longitudinal and Vertical Rail Modes

Figure 1.9 shows the power spectra of the calculated wear under different corrugation amplitudes. When  $A = 20 \mu\text{m}$ , a major frequency component is observed at approximately 1296 Hz, approaching the corrugation passing frequency of 1297 Hz (estimated with a wheel passing at 38.9 m/s over the corrugation with a wavelength of 30 mm). When  $A$  is reduced, this major frequency also decreases. At  $A = 2.5 \mu\text{m}$ , the frequency is 1290 Hz, which is 7 Hz lower. Thus, the frequency of the wear is initially (i.e., when  $A$  is small) lower than that of the modeled corrugation, and it is influenced by the corrugation.

When  $A$  is increased to  $20\ \mu\text{m}$ , there is a sudden PSD increase at  $1185\ \text{Hz}$ ; see the second major peak in Figure 1.9. Modal analysis in Figure 1.10a,b shows that these two major frequencies of  $1185$  and  $1296\ \text{Hz}$  correspond to two natural frequencies of the system ( $1185\ \text{Hz}$  of a vertical rail mode and  $1291\ \text{Hz}$  of a longitudinal rail mode), i.e., the two natural frequencies that are closest to and/or lower than the corrugation passing frequency of  $1297\ \text{Hz}$  (see in Figure 1.10 the characteristic modal shapes). The closest pin-pin resonance is at approximately  $1110\ \text{Hz}$  (Figure 1.10c), and it thus does not seem to have influence on the wear development in this case.

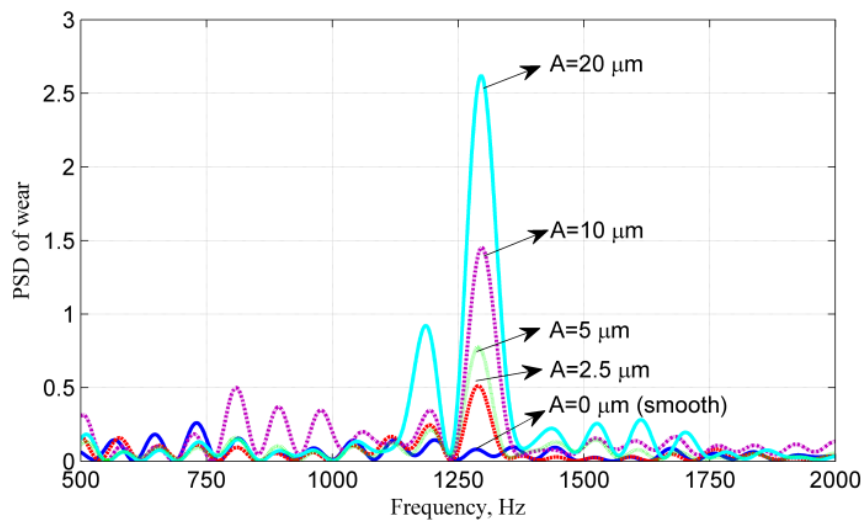


Figure 1.9. Power spectral density (PSD) of wear  $\lambda = 30\ \text{mm}$ , with a major peak at  $1296\ \text{Hz}$  and a secondary peak at  $1185\ \text{Hz}$ , when  $A = 20\ \mu\text{m}$ .

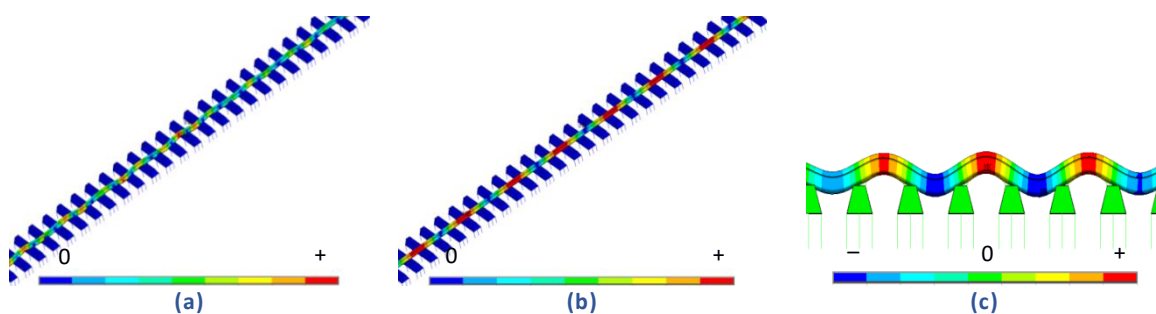


Figure 1.10. Modal analysis of the two major frequencies ( $1185$  and  $1296\ \text{Hz}$ ) shown in Figure 1.9: (a) rail vertical mode at  $1185\ \text{Hz}$  and (b) rail longitudinal mode at  $1291\ \text{Hz}$ , in comparison with the closest vertical pin-pin mode at  $1100\ \text{Hz}$  shown in (c).

Based on Figure 1.9, it is reasonable to assume that the development of the observed corrugation with a wavelength of  $30\ \text{mm}$  is mainly related to these two modes. Then, the track parameters are a stronger determinant of the corresponding wavelength of the calculated wear than is the modeled corrugation because the track parameters determine the longitudinal and vertical modes.



When the corrugation amplitude is close to zero, e.g.,  $A = 2.5 \mu\text{m}$  or less, the major frequency of the wear is approximately 1290 Hz, which is 6 Hz lower than the 1296 Hz of the wear at  $A = 20 \mu\text{m}$ , 1 Hz lower than the longitudinal modes, but 105 Hz higher than the vertical mode. This suggests that for the initiation of corrugation, the longitudinal mode should have played a major role compared with the vertical mode. Additionally, the periodic wear under the smooth rail condition has one peak at 1290 Hz. When the amplitude of corrugation is progressively increased, the differential wear at this frequency grows consistently. This phenomenon does not happen at the other frequencies. This implies a positive-feedback process taking place at around this frequency. Besides, in Figure 1.9, the series of peaks from  $A = 20 \mu\text{m}$  and further to the smooth rail converge asymptotically to the smooth rail situation of  $A = 0 \mu\text{m}$ . Based on the positive feedback and trend analysis, it is reasonable to infer that the longitudinal vibration modes are probably dominant for short pitch corrugation initiation. In the corrugation initiation, the longitudinal modes in the form of compression and rarefaction waves influence the local wheel-rail contact of forces and creepage and result in their fluctuation and thus the formation of the differential wear.

With the growth of corrugation, the vertical mode plays an increasingly important role. This behavior is confirmed by Figure 1.9: when  $A$  is larger than  $10 \mu\text{m}$ , the PSD peak of the secondary frequency at 1185 Hz begins to make a significant contribution to the wear. This frequency corresponds to the vertical mode and is excited when the corrugation amplitude is sufficiently large. When the corrugation amplitude is further increased, it will incur wear that is of the same frequency as the corrugation. Therefore, when the corrugation amplitude is significant, the vertical modes will be dominant.

For intermediate situations, the longitudinal and vertical modes together determine whether corrugation will grow or be suppressed by wear based on whether the wear is of the same frequency and correct phase. In other words, when the vertical and longitudinal modes are inconsistent, the differential wear caused by the respective modes will suppress each other so that there will be no corrugation, no matter high or low adhesion, as long as the consistency condition is not satisfied. Certain track parameters could satisfy the required consistency requirement; thus, corrugation will appear in some places, but not in others.

In summary, the longitudinal vibration modes are probably dominant for short pitch corrugation initiation. Then, the interaction and consistency between longitudinal and vertical modes should determine the development of short pitch corrugation, and once a certain severity is reached, vertical modes become dominant. This global perspective of the consistency conditions that govern the evolution of short pitch corrugation represents a novel contribution. The literature has so far only considered the effects of the vertical, lateral and torsional modes [1,3,39,40,56,57]. In [42], the relative longitudinal vibration of the two rails of a track is considered for corrugation initiation, for which each half track is modelled as an inertia, and longitudinal vibration modes of the rail as a flexible body are not considered.

#### 1.4.4 Additional Comments

Minor frequency components may also be relevant. According to the previous analysis, the wavelength of the wear changes with the corrugation amplitude  $A$ ; however, Figure 1.8a shows a constant wear wavelength because Figure 1.8a was high-pass filtered at  $\lambda = 20$  mm. When the same signals are high-pass filtered at  $\lambda = 30$  mm, i.e., when the frequencies of 1185 Hz and 1291 Hz are given a more dominant role, the wavelength also varies (Figure 1.8b), and the phase of the wear changes with  $A$ . This behavior indicates that certain minor frequency components of wear shown in Figure 1.9 also play a relevant role in determining the wavelength and phase of the wear and thus the development of corrugation.

Studying corrugation by pre-selecting certain modes may lead to different and possibly non-physical results, thereby highlighting the subtleness of the corrugation problem. However, this also reveals one of the advantages of the proposed modeling approach, which can contain all necessary modes of the structure and continua in the system by modeling the relevant components and interfaces with realistic geometry and material properties. Several questions for further research could focus on the cut-off wavelength for filtering: what is the shortest cut-off wavelength for filtering? Could it be related to the shortest observed corrugation wavelength of 20 mm? Is the optimal cut-off frequency equal to 20 mm or should it be shorter? Is this frequency related to the concept of the contact filter [58]?

According to the above discussion, instead of increasing to 1296 Hz, the major frequency in Figure 1.9 should decrease from 1290 Hz at  $A = 2.5$   $\mu\text{m}$  toward the frequency of the vertical mode of 1185 Hz when the corrugation amplitude grows and the vertical mode becomes dominant. This mismatch is caused by the inconsistency between the modeled corrugation wavelength of 30 mm and the natural modes of the track, which are determined by the nominal track parameters used in the modeling. The prescribed wavelength is a field observation related to deviation from the nominal track. The nominal track parameters do not necessarily cause corrugation; otherwise, corrugation would be observed everywhere. Because of this mismatch, the calculated wear tends to erase the corrugation.

### 1.5 Relationship between Contact Forces and Wear as well as New Insights

Based on the discussion in Section 1.4, it may be inferred that equal longitudinal and vertical natural frequencies may represent a condition for corrugation to consistently initiate and grow; this may be achieved by properly constraining the rail by the fastening system [59]. The next question is whether corrugation occurs at certain preferred frequencies. Because the natural modes should be excited by contact forces and dynamic contact forces are caused by corrugation, the effects of the prescribed corrugation on the normal and longitudinal forces are examined below. Note that for corrugation, the difference between the vertical and normal directions of wheel-rail contact is negligible.

### 1.5.1 Normal and Longitudinal Forces Do Not Exactly Follow Corrugation in Wavelength and Phase

Figure 1.11 shows the normal contact force ( $F_N$ ) and longitudinal contact force ( $F_L$ ) when the rail is smooth and when corrugation is present. Although the wavelength of the modeled corrugation is constant (30 mm), the wavelengths of the resulting dynamic wheel-rail contact forces vary along the rail (Figure 1.11a). Specifically,  $F_N$  initially lags behind the corrugation, i.e., the peak of  $F_N$  appears to the left side of the corresponding corrugation peak. When approaching the sleeper, which has a width of 140 mm and is centered at 1.20 m, the force catches up and becomes in phase with the corrugation at approximately 1.1 m, i.e., near the edge of the sleeper. The force subsequently tends to lead the corrugation. A similar situation applies to  $F_L$  (Figure 1.11b). However,  $F_N$  leads  $F_L$  initially, and the two forces later tend to be in phase at approximately 1.23 m, with subsequent lagging of  $F_N$ . Note that the wear is also strongest at approximately 1.23 m (according to Section 1.4.2).

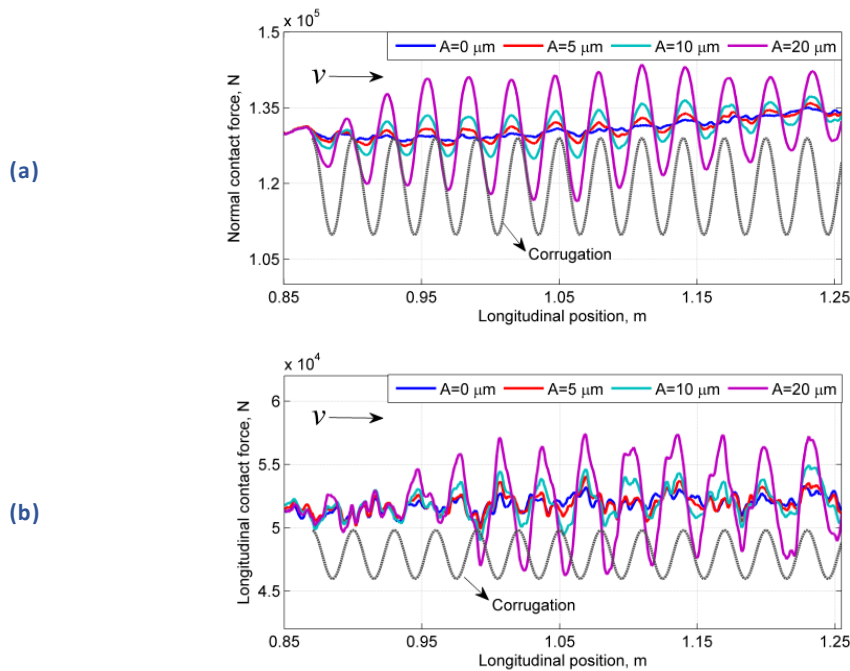


**Figure 1.11. Dynamic wheel-rail contact forces obtained for the corrugation in Figure 1.3 with  $\theta = 0$  and P4 at 1.2 m (1.2 m is in the middle of a sleeper and 0.9 m is at the midpoint between two sleepers.). (a) Normal contact force. (b) Longitudinal contact force.**

The PSD analysis in Figure 1.12a reveals that the main frequency components of  $F_N$  and  $F_L$  are 1257 Hz and 1226 Hz, respectively. The corresponding vertical and longitudinal rail vibration modes closest to the corrugation passing frequency of 1297 Hz are 1185 and 1291 Hz, which means that the normal and longitudinal contact forces do not exactly follow the excitation and have frequencies that are different from the natural vibration modes. Previous studies have either explicitly or implicitly assumed that the frequencies of the longitudinal contact force, the normal contact force and the

vertical natural mode are the same as the corrugation passing frequency; however, the longitudinal mode has not been previously considered.

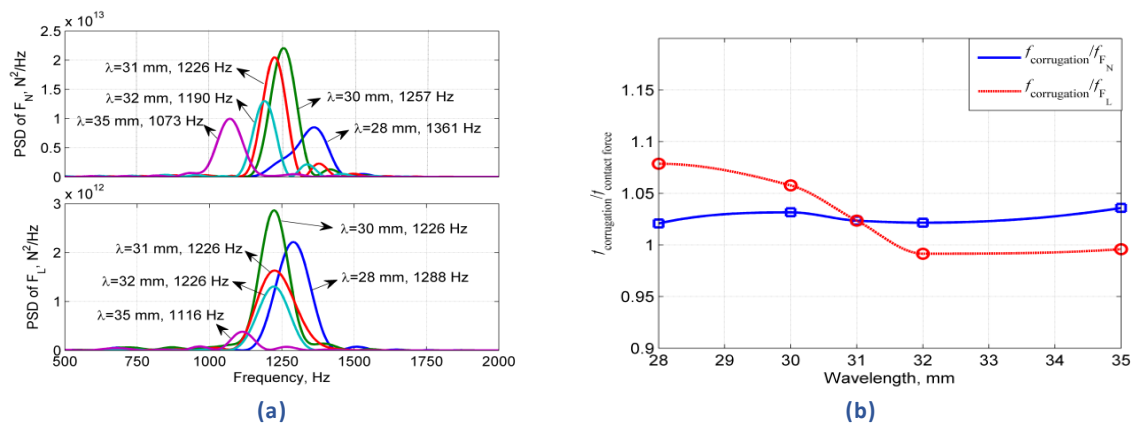


**Figure 1.12. Relationships between the PSD and frequencies of the contact forces and corrugation wavelength obtained for the corrugation in Figure 1.3b with  $\theta = 0$ , P4 at 1.2 m and  $A = 20 \mu\text{m}$ . Note that in (b),  $f_{\text{corrugation}}$  is not constant, but changes with the corrugation wavelength. Thus, although the PSD of FL varies in a narrower band than FN in (a), the opposite pattern is observed in (b). (a) PSD of FN (upper) and FL (lower). (b) Ratio of corrugation over contact force frequency.**

### 1.5.2 Preferred Frequency of Contact Forces

The dynamic normal and longitudinal contact forces are determined by the combined effects of the parameters of the structure, the excitation by the corrugation and the transient rolling contact. To investigate the contact force sensitivity to different corrugation wavelengths, the wavelength is varied at 28, 30, 31, 32 and 35 mm. Figure 1.12 shows the relationships between the PSD and frequencies of the contact forces and the corrugation wavelength. The following observations can be made.

- (1) The frequencies of the normal and longitudinal forces are different. The frequencies of the contact forces are different from that of the excitation, i.e., the passing frequency of the corrugation, and they are sensitive to and change with the corrugation wavelengths. The dynamic forces are stronger at certain wavelengths than others. With the current track parameters, both the longitudinal and vertical contact forces are strongest at  $\lambda = 30$  mm. This again is in agreement with the observed corrugation wavelength of 30 mm.
- (2) The bandwidth of the frequency change of the longitudinal force is between 1116 Hz and 1288 Hz (Figure 1.12a), which is narrower than that of the normal force (between 1073 and 1361 Hz). The frequency band of the vertical force is broader because it follows the change in the corrugation wavelength, as shown in Figure 1.12b for the relatively constant ratio of the corrugation passing frequency to the contact force frequency. The frequency of the longitudinal contact force is lower than that of the normal contact force when the corrugation

wavelength is short, i.e., between  $\lambda = 28$  mm and 31 mm (Figure 1.12b), and vice versa when the corrugation wavelength is longer than 31 mm.

(3) The frequency of the normal contact force is always lower than that of the excitation (Figure 1.12b). The presence of corrugation is an excitation mainly in the normal direction; thus, the response always follows the excitation. However, the frequency of the longitudinal contact force can be lower or higher than that of the excitation, which likely depends on the nearest natural frequency, as well as the complex relationship between the tangential and normal contact forces. This pattern reveals a strong dependence of the normal contact force on the excitation and a relatively weaker dependence of the longitudinal contact force on the excitation. These dependencies are in line with the narrower band of the frequency change of the longitudinal force compared with the normal force.

(4) In Figure 1.12b, the frequency of the longitudinal contact force has the largest deviation from the corrugation passing frequency when the wavelength is shorter, i.e., at  $\lambda = 28$  mm. With increasing  $\lambda$ , the deviation decreases. At approximately  $\lambda = 31.5$  mm, the frequency of the longitudinal contact force equals the passing frequency. The longitudinal contact force subsequently follows the excitation closely.

(5) The frequency curves (Figure 1.12b) of the normal and longitudinal contact forces cross each other at a wavelength of 31 mm, where the frequencies of the normal and longitudinal forces are equal. Is an equal frequency of the two forces a condition for the corrugation to initiate, grow and become a wavelength-fixing mechanism? As shown in Sections 1.4.2 and 1.5.1, the wear is strongest when the normal and longitudinal forces  $F_N$  and  $F_L$  are in phase at 1.23 m. Because an equal frequency is a necessary condition for  $F_N$  and  $F_L$  to be in phase over many wavelengths, it is indeed a favorable condition for corrugation development.

These observations indicate that the system appears to have a preference for certain frequencies, which is further confirmed by Figure 1.12a, in which the frequency of the longitudinal contact force is 1226 Hz for  $\lambda = 30$  mm, 31 mm and 32 mm. This apparent preference is also in agreement with the results of [3], which show that most models in the literature suggest a fixed frequency related to vertical resonances in the system. However, this preference appears contrary to the hypothesis of fixed wavelength [1] and is part of the enigma of the corrugation problem: is the mechanism underlying corrugation a wavelength-fixing or frequency-fixing mechanism [3]?

### 1.5.3 Frequencies Converge to Develop Uniform Corrugation

Equal longitudinal and vertical natural frequencies have been shown to represent preferred conditions under which corrugation can initiate and grow; thus, it is reasonable to infer that the frequencies of the related contact forces and the resulting wear are also equal, such that the five different frequencies converge to one frequency: the corrugation passing frequency. Therefore, the frequency appears to be fixed at a preferred resonance, whereas the wavelength is “fixed” in the sense that it can vary only in a small range. This supposition explains the observations in Section 1.5.2, in which the

frequency converges to 1226 Hz, while the preferred wavelength varies because of the mismatch between the given corrugation wavelength and the nominal track parameters. The strongest contact forces are at  $\lambda = 30$  mm; the frequencies of the longitudinal and normal forces are equal at  $\lambda = 31$  mm; and the frequency of the longitudinal force and the corrugation passing frequency are equal at  $\lambda = 31.5$  mm.

It is also reasonable to infer that when the track parameters that caused the observed corrugation are known and the mismatch between the model input and the prescribed corrugation is eliminated, all of the different wavelengths will converge to the observed wavelength of 30 mm if the traffic speed is 140 km/h, which implies that varying traffic speed can suppress corrugation by changing the wavelength as was shown in [60]. The problem for further research now becomes modeling degraded track to identify the track parameters at which the system converges to the preferred frequencies and wavelengths with a phase angle of wear that promotes corrugation growth at every wheel passage.

#### 1.5.4 Importance of the Proposed Modeling Approach and Track Parameters

Since the foundational work of Grassie [61–63], modeling corrugation has generally been based on wheel and rail sub-models that consist of beams and plates, and the wheel-rail contact is solved separately via statics and then coupled to the wheel-rail system. These calculations were limited by the state of the art. For contact mechanics, “the mechanics of steady or slowly varying creep forces has been very thoroughly studied, but the behavior under transient or rapidly oscillating conditions is virtually unexplored” [63]. The longitudinal dynamics of the wheel-rail interaction were investigated experimentally in [62], and longitudinal resonances higher than 900 Hz were observed. Such resonances were not considered important and thus were ignored in further investigations, and the focus for corrugation has been on vertical, lateral and wheelset torsional dynamics [1,3,39,40,56,57]. In this chapter, by analyzing the frictional rolling in the vehicle-track system under transient and rapidly oscillating conditions, the influence of both the vertical and the longitudinal vibration modes on corrugation initiation and growth was captured. However, further research should be performed that includes the influence of the track structure, especially the fastening, which plays a major role in constraining the rail and affecting its modes [59]. Studies have modelled fastenings and sleepers and identified their parameters [19,50,64,65], and these works have revealed that the alignment of the fastening system influences the frequency of normal and longitudinal dynamics and that the natural frequencies are determined by the system parameters.

Figure 1.1 shows different cases of corrugations under different track types, i.e., mono-block sleeper versus duo-block sleeper and W-shaped tension clamp versus Deenik clips. Among the three figures in Figure 1.1, Figure 1.1a is at a gentle curve, and the latter two figures are on straight tracks. These observations agree with the description of the short pitch corrugation [1]. Comparing the three photos reveals that the characteristics of the corrugation differ from track to track. Certain corrugations are more or less uniformly distributed along the track (Figure 1.1a), whereas others are more severe near the sleeper support (Figure 1.1b,c). The difference between Figure 1.1a and Figure 1.1b,c is the types of sleepers and fastenings. According to Figure 1.1b, the wavelength of the corrugation may vary

significantly within a sleeper span. Moreover, Figure 1.1b,c is from the same track, thus having the same traffic and same types of sleeper and fastening; however, large differences in the corrugations are apparent. These observations all indicate that corrugation is sensitive to track conditions, thus highlighting directions for future work.

### 1.5.5 Additional Discussions

In this section, 2D and 3D analysis results are briefly compared. In [16], a 2D non-Hertzian contact model is developed in which the stress distribution is not symmetric at the falling and rising edges of the corrugation. The same phenomenon is observed in the present 3D numerical analysis. A clear difference between the 2D and 3D approaches is that in the 2D analysis, the contact patches at the falling and rising edges are symmetric in the longitudinal direction about the contact patch center. In the case of the 3D analysis, the contact patches are not symmetric about the contact patch center.

As shown in Figure 1.11a, approximately two wavelengths are required for the normal contact force to transit from the steady state before the corrugation, which starts at 0.87 m, to the new steady state controlled by the corrugation. For the tangential force, approximately 3.5 wavelengths are required. Thus, the longitudinal force lags approximately 1.5 wavelengths behind the normal force, i.e., approximately 45 mm. Because the length of the contact patch is approximately 15 mm (see Figure 1.6), the lag is approximately three-times the length of a contact patch. In [14], the lag for static rolling contact is one length of a contact patch, which reveals another difference between static and dynamic rolling contact. Moreover, Figure 1.11 shows that the tangential contact force contains considerably more harmonics than the normal force.

Metallurgical investigations on corrugated rail material show that the corrugation crest experiences high dynamic contact forces, high deformation, work hardening and, consequently, high wear resistance. The corrugation trough, instead, is reported to be developed from wear [11,52]. This is in agreement with the numerical results in the present chapter, i.e., high contact pressure is found at the corrugation crest and lower pressure and high micro-slip at the corrugation trough. Additionally, the delay in corrugation growth with reduction of wear by friction modifier [66] also supports wear as a mechanism of the corrugation.

Although more research using more sophisticated models for the longitudinal support is needed, the findings of this chapter have relevance for the numerical modeling of longitudinal modes. The inclusion of longitudinal support stiffness, such as in [62], results in a longitudinal mode at approximately 1298 Hz, which represents a difference of 7 Hz with respect to the model without longitudinal rail support. Hence, the more complex model does not result in a significant difference in the longitudinal dynamics. This situation should be further explored by investigating the actual parameters experimentally under Dutch conditions and verifying the dynamics.

## 1.6 References

- [1] Grassie, S.L. Rail corrugation: Characteristics, causes, and treatments. *Proc. Inst. Mech. Eng. Part F J. Rail Rapid Transit* 2009, 223, 581–596.
- [2] Sato, Y.; Matsumoto, A.; Knothe, K.L. Review on rail corrugation studies. *Wear* 2002, 253, 130–139.
- [3] Afferrante, L.; Ciavarella, M. Short pitch corrugation of railway tracks with wooden or concrete sleepers: An enigma solved? *Tribol. Int.* 2010, 43, 610–622.
- [4] Meehan, P.A.; Bellette, P.A.; Horwood, R.J. “Does god play dice with corrugations?”: Environmental effects on growth. *Wear* 2014, 314, 254–260.
- [5] Giannakos, K. Modeling the influence of short wavelength defects in a railway track on the dynamic behavior of the non-suspended masses. *Mech. Syst. Signal Process.* 2016, 68, 68–83.
- [6] Tavares de Freitas, R.; Kaewunruen, S. Life Cycle Cost Evaluation of Noise and Vibration Control Methods at Urban Railway Turnouts. *Environments* 2016, 3, 34, doi:10.3390/environments3040034.
- [7] Li, Z.; Zhao, X.; Esveld, C.; Dollevoet, R.; Molodova, M. An investigation into the causes of squats—correlation analysis and numerical modelling. *Wear* 2008, 265, 1349–1355.
- [8] Nielsen, J.C.O. Numerical prediction of rail roughness growth on tangent railway tracks. *J. Sound Vib.* 2003, 267, 537–548.
- [9] Xie, G.; Iwnicki, S.D. Calculation of wear on a corrugated rail using a three-dimensional contact model. *Wear* 2008, 265, 1238–1248.
- [10] Böhmer, A.; Klimpel, T. Plastic deformation of corrugated rails—A numerical approach using material data of rail steel. *Wear* 2002, 253, 150–161.
- [11] Baumann, G.; Fecht, H.J.; Liebelt, S. Formation of white-etching layers on rail treads. *Wear* 1996, 191, 133–140.
- [12] Li, Z.; Zhao, X.; Dollevoet, R.; Molodova, M. Differential wear and plastic deformation as causes of squat at track local stiffness change combined with other track short defects. *Veh. Syst. Dyn.* 2008, 46, 237–246.
- [13] Saulot, A.; Descartes, S.; Berthier, Y. Sharp curved track corrugation: From corrugation observed on-site, to corrugation reproduced on simulators. *Tribol. Int.* 2009, 42, 1691–1705.
- [14] Kalker, J.J. *Three-Dimensional Elastic Bodies in Rolling Contact*; Kluwer: Dordrecht, The Netherlands, 1990.
- [15] Li, Z. *Wheel-Rail Rolling Contact and Its Application to Wear Simulation*. Ph.D. Thesis, Delft University of Technology, Delft, The Netherlands, 2002.
- [16] Nielsen, J.B. Evolution of rail corrugation predicted with a nonlinear wear model. *J. Sound Vib.* 1999, 227, 915–933.



- [17] Shen, Z.; Li, Z. A fast non-steady state creep force model based on the simplified theory. *Wear* 1996, 191, 242–244.
- [18] Knothe, K.; Groß-Thebing, A. Short wavelength rail corrugation and non-steady-state contact mechanics. *Veh. Syst. Dyn.* 2008, 46, 49–66.
- [19] Ilias, H. The influence of railpad stiffness on wheelset/track interaction and corrugation growth. *J. Sound Vib.* 1999, 227, 935–948.
- [20] Jin, X.; Wen, Z. Effect of discrete track support by sleepers on rail corrugation at a curved track. *J. Sound Vib.* 2008, 315, 279–300.
- [21] Grassie, S.L. Squats and squat-type defects in rails: The understanding to date. *Proc. Inst. Mech. Eng. Part F J. Rail Rapid Transit* 2012, 226, 235–242.
- [22] Hempelmann, K.; Knothe, K. An extended linear model for the prediction of short pitch corrugation. *Wear* 1996, 191, 161–169.
- [23] Saulot, A.; Baillet, L. Dynamic finite element simulations for understanding wheel-rail contact oscillatory states occurring under sliding conditions. *J. Tribol. ASME* 2006, 128, 761–770.
- [24] Zhao, X.; Li, Z. The solution of frictional wheel-rail rolling contact with a 3D transient finite element model: Validation and error analysis. *Wear* 2011, 271, 444–452.
- [25] Nishiura, D.; Sakaguchi, H.; Aikawa, A. Development of Viscoelastic Multi-Body Simulation and Impact Response Analysis of a Ballasted Railway Track under Cyclic Loading. *Materials* 2017, 10, 615, doi:10.3390/ma10060615.
- [26] Li, S.; Li, Z.; Dollevoet, R. Wear study of short pitch corrugation using an integrated 3D FE train-track interaction model. In *Proceedings of the 9th International Conference on Contact Mechanics and Wear of Rail/Wheel Systems, Chengdu, China, 27–30 August 2012*; pp. 216–222.
- [27] Zhao, X.; Wen, Z.; Wang, H.; Jin, X.; Zhu, M. Modeling of high-speed wheel-rail rolling contact on a corrugated rail and corrugation development. *J. Zhejiang Univ. Sci. A* 2014, 15, 946–963.
- [28] Zhao, X.; Li, Z. A three-dimensional finite element solution of frictional wheel-rail rolling contact in elasto-plasticity. *Proc. Inst. Mech. Eng. Part F J. Rail Rapid Transit* 2015, 229, 86–100.
- [29] Hiensch, M.; Nielson, J.C.O.; Verherjen, E. Rail corrugation in The Netherlands—Measurements and simulations. *Wear* 2002, 253, 140–149.
- [30] Molodova, M.; Li, Z.; Núñez, A.; Dollevoet, R. Validation of a finite element model for axle box acceleration at squats in the high frequency range. *Comput. Struct.* 2014, 141, 84–93.
- [31] Arias-Cuevas, O.; Li, Z.; Lewis, R. Investigating the lubricity and electrical insulation caused by sanding in dry wheel-rail contacts. *Tribol. Lett.* 2010, 37, 623–635.
- [32] Cann, P.M. The “leaves on the line” problem—A study of leaf residue film formation and lubricity under laboratory test conditions. *Tribol. Lett.* 2006, 24, 151–158.

- [33] Courant, R.; Friedrichs, K.O.; Lewy, H. On the partial difference equations of mathematical physics. *IBM J.* 1967, 11, 215–234.
- [34] Benson, D.J.; Hallquist, J.O. A single surface contact algorithm for the post buckling analysis of shell structures. *Comput. Methods Appl. Mater Eng.* 1990, 78, 141–163.
- [35] Popovici, R. Friction in Wheel-Rail Contacts. Ph.D. Thesis, University of Twente, Enschede, The Netherlands, 2010.
- [36] Bhushan, B. *Modern Tribology Handbook: Principles of Tribology*; CRC Press: Boca Raton, FL, USA, 2001.
- [37] Oostermeijer, K.H. Review on short pitch rail corrugation studies. *Wear* 2008, 265, 1231–1237.
- [38] Liu, Q.; Zhang, B.; Zhou, Z. An experimental study of rail corrugation. *Wear* 2003, 255, 1121–1126.
- [39] Collette, C.; Horodincu, M.; Preumont, A. Rotational vibration absorber for the mitigation of rail rutting corrugation. *Veh. Syst. Dyn.* 2009, 47, 641–659.
- [40] Tassilly, E.; Vincent, N. A linear model for the corrugation of rails. *J. Sound Vib.* 1991, 150, 25–45.
- [41] Li, W.; Wang, H.; Wen, Z.; Du, X.; Wu, L.; Li, X.; Jin, X. An investigation into the mechanism of metro rail corrugation using experimental and theoretical methods. *Proc. Inst. Mech. Eng. Part F J. Rail Rapid Transit* 2016, 230, 1025–1039.
- [42] Hayes, W.F.; Tucker, H.G. Wheelset-track resonance as a possible source of corrugation wear. *Wear* 1991, 144, 211–226.
- [43] Suda, Y.; Komine, H.; Iwasa, T.; Terumichi, Y. Experimental study on mechanism of rail corrugation using corrugation simulator. *Wear* 2002, 253, 162–171.
- [44] Jin, X.; Xiao, X.; Wen, Z.; Zhou, Z. Effect of sleeper pitch on rail corrugation at a tangent track in vehicle hunting. *Wear* 2008, 265, 1163–1175.
- [45] Grassie, S.L.; Johnson, K.L. Periodic microslip between a rolling wheel and a corrugated rail. *Wear* 1985, 101, 291–309.
- [46] Bellette, P.A.; Meehan, P.A.; Daniel, W.J.T. Effects of variable pass speed on wear-type corrugation growth. *J. Sound Vib.* 2008, 314, 616–634.
- [47] Knothe, K.L.; Grassie, S.L. Modelling of railway track and vehicle/track interaction at high frequencies. *Veh. Syst. Dyn.* 1993, 22, 209–262.
- [48] Li, Z.; Dollevoet, R.; Molodova, M.; Zhao, X. Squat growth—Some observations and the validation of numerical predictions. *Wear* 2011, 271, 148–157.
- [49] Wei, Z.; Li, Z.; Qian, Z.; Chen, R.; Dollevoet, R. 3D FE modelling and validation of frictional contact with partial slip in compression-shift-rolling evolution. *Int. J. Rail Transp.* 2015, 4, 20–36.
- [50] Oregui, M.; Li, Z.; Dollevoet, R. An investigation into the vertical dynamics of tracks with monoblock sleepers with a 3D finite-element model. *Proc. Inst. Mech. Eng. Part F J. Rail Rapid Transit* 2016, 230, 891–908.

- [51] Molodova, M. Detection of Early Squats by Axle Box Acceleration. Ph.D. Thesis, Delft University of Technology, Delft, The Netherlands, 2013.
- [52] Feller, H.G.; Waif, K. Surface analysis of corrugated rail treads. *Wear* 1991, 144, 153–161.
- [53] Jin, X.; Wen, Z.; Wang, K.; Zhang, W. Effect of a scratch on curved rail on initiation and evolution of rail corrugation. *Tribol. Int.* 2004, 37, 385–394.
- [54] Igeland, A. Railhead corrugation growth explained by dynamic interaction between track and bogie wheelsets. *Proc. Inst. Mech. Eng. Part F J. Rail Rapid Transit* 1996, 210, 11–20.
- [55] Archard, J.F. Contact and rubbing of at surfaces. *J. Appl. Phys.* 1953, 24, 981–988.
- [56] Tassilly, E.; Vincent, N. Rail corrugation: Analytical model and field tests. *Wear* 1991, 144, 163–178.
- [57] Ahlbeck, D.R.; Daniels, L.E. Investigation of rail corrugations on the Baltimore metro. *Wear* 1991, 144, 197–210.
- [58] Remington, P.J. Wheel/rail noise-part IV: Rolling noise. *J. Sound Vib.* 1976, 46, 419–436.
- [59] Zhao, X.; Li, Z.; Dollevoet, R. Influence of the fastening modeling on the vehicle-track interaction at singular rail surface defects. *J. Comput. Nonlinear Dyn.* 2014, 9, 031002.
- [60] Meehan, P.A.; Batten, R.D.; Bellette, P.A. The effect of non-uniform train speed distribution on rail corrugation growth in curves/corners. *Wear* 2016, 366, 27–37.
- [61] Grassie, S.L.; Gregory, R.W.; Harrison, D.; Johnson, K.L. The dynamic response of railway track to high frequency vertical excitation. *J. Mech. Eng. Sci.* 1982, 24, 77–90.
- [62] Grassie, S.L.; Gregory, R.W.; Johnson, K.L. The dynamic response of railway track to high frequency longitudinal excitation. *J. Mech. Eng. Sci.* 1982, 24, 97–102.
- [63] Grassie, S.L.; Gregory, R.W.; Johnson, K.L. The behaviour of railway wheelsets and track at high frequencies of excitation. *J. Mech. Eng. Sci.* 1982, 24, 103–111.
- [64] Egana, J.I.; Vinolas, J.; Seco, M. Investigation of the influence of rail pad stiffness on rail corrugation on a transit system. *Wear* 2006, 261, 216–224.
- [65] Oregui, M.; Núñez, A.; Dollevoet, R.; Li, Z. Sensitivity analysis of railpad parameters on vertical railway track dynamics. *J. Eng. Mech.* 2017, 143, 04017011, doi:10.1061/(ASCE)EM.1943-7889.0001207.
- [66] Egana, J.I.; Vinolas, J.; Gil-Negrete, N. Effect of liquid high positive friction (HPF) modifier on wheel-rail contact and rail corrugation. *Tribol. Int.* 2005, 38, 769–774.

## 2 Catalogue of Corrugation in Turkey

### 2.1 Brief summary about the corrugation catalogue

To understand the influence of parameters in corrugation, a corrugation catalogue in Turkey is developed. The catalogue is formed by taking into account the existing information taken from the headquarter and regional directorates of TCDD. Thereof, as seen in Figure 2.1, a specific photo (as left and right rails), track parameters and traffic situation are described.

The catalogue divided into three sections: Corrugation, track parameters and traffic. The parameters for each type are given in Table 1.

**Table 2.1.1 Diversification of parameters according to sections in catalogue template**

Corrugation Section	Track Parameters	Traffic
<ul style="list-style-type: none"> <li>▪ Wavelength</li> <li>▪ Amplitude</li> <li>▪ Type of Corrugation</li> </ul>	<ul style="list-style-type: none"> <li>▪ Type of Rail</li> <li>▪ Rail Grade</li> <li>▪ Type of Sleepers</li> <li>▪ Type of Fastening System</li> <li>▪ Type of Rail Pad</li> <li>▪ Curvature (Straight / Curve)</li> <li>▪ Lubrication Condition</li> <li>▪ Date of Renewal/ Reparation</li> </ul>	<ul style="list-style-type: none"> <li>▪ Type of Traffic</li> <li>▪ Single/ Double Traffic Direction</li> <li>▪ Axle Load of Passenger Trains</li> <li>▪ Axle Load of Freight Trains</li> <li>▪ Speed Limit for Passenger Trains</li> <li>▪ Speed Limit for Freight Trains</li> <li>▪ Vehicle Velocity</li> <li>▪ Vehicle in Acceleration</li> <li>▪ Vehicle in Deceleration</li> <li>▪ Number of Daily Passenger Trains</li> <li>▪ Number of Freight Trains</li> <li>▪ Gross Ton (Annually)</li> </ul>

The name of the lines is detected corrugations are:

- Alayunt – Eskişehir (17+150 km; 17+220 km)
- Çerikli – Kırıkkale (138+500 km)
- Çerikli – Yerköy (203+100 km)

The corrugation classification according to wavelength:

- Short pitch corrugation (30-100 mm)
- Medium pitch corrugation (100-300 mm)
- Long pitch corrugation (wavelength > 300 mm)

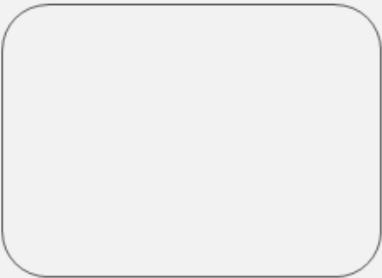
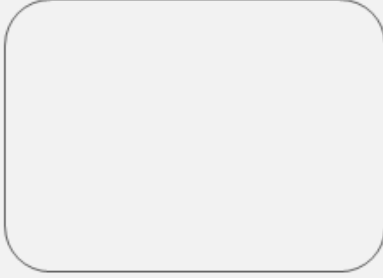
<i>CORRUGATION CATALOGUE</i>		<i>NETIRAIL-INFRA 636237</i>	
<b><u>TYPE OF CORRUGATION:</u></b>			
			
<b>CORRUGATION</b>		<b>TRAFFIC</b>	
Wavelength		Type of Traffic	
Amplitude		Single/ Double Traffic Direction	
Type of Corrugation		Axle Load of Passenger Trains	
<b>TRACK PARAMETERS</b>		Axle Load of Freight Trains	
Type of Rail		Speed Limit for Passenger Trains	
Rail Grade		Speed Limit for Freight Trains	
Type of Sleepers		Vehicle Velocity	
Type of Fastening System		Vehicle in Acceleration	
Type of Rail Ped		Vehicle in Deceleration	
Curvature (Straight/Curve)		Number of Daily Passenger Trains	
Lubrication Condition		Number of Freight Trains	
Date of Renewal/ Reparation		Gross Ton (Annually)	
1			

Figure 2.1 Developed template for TCDD corrugation catalogue

## 2.2 Examples of the corrugation catalogue

Few examples of the corrugation catalogue are given as short pitch, medium pitch and long pitch in below Figures.

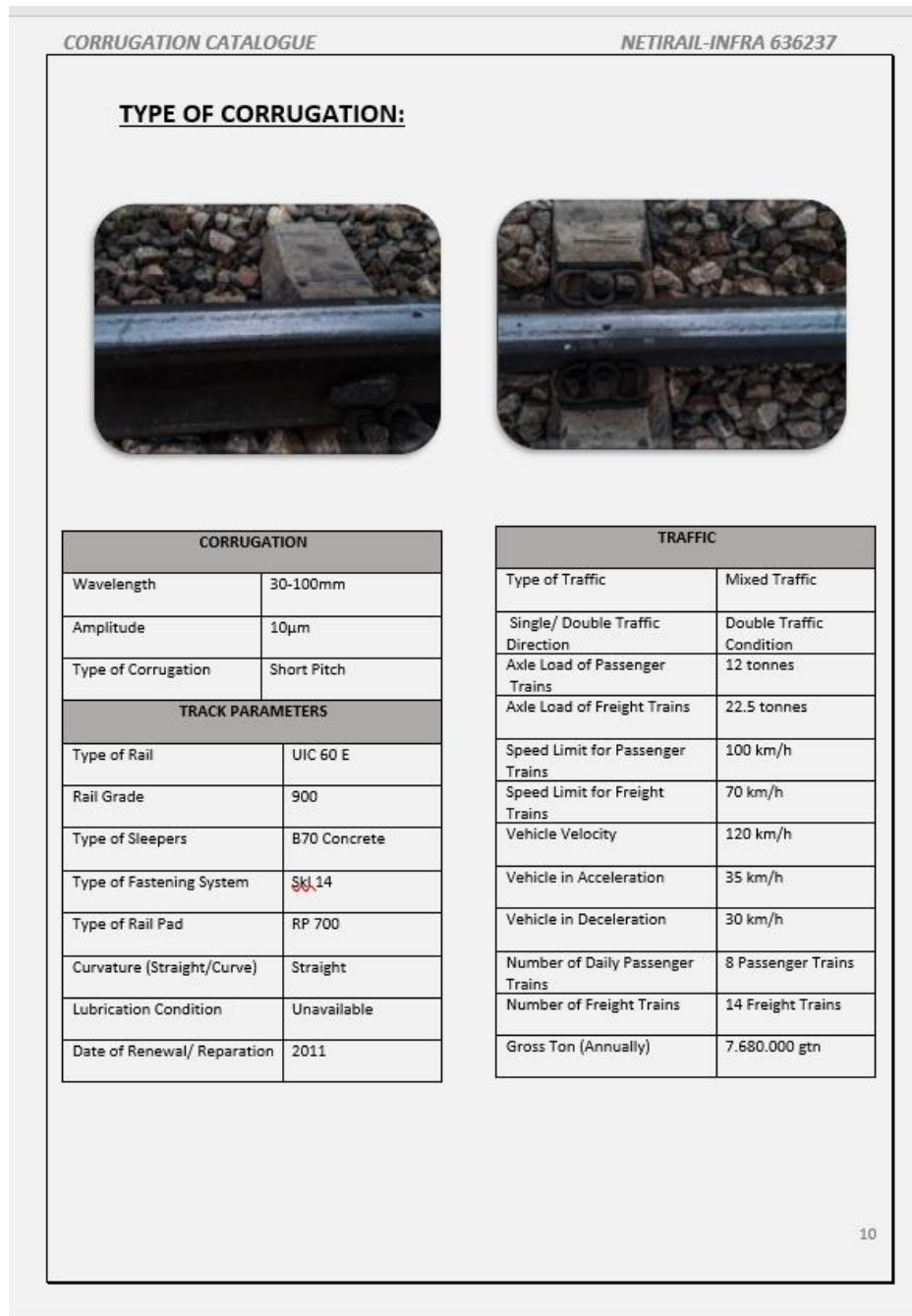


Figure 2.2.1 An example of TCDD corrugation catalogue (short-pitch corrugation)



Figure 2.2.2 An example of TCDD corrugation catalogue (medium pitch corrugation)

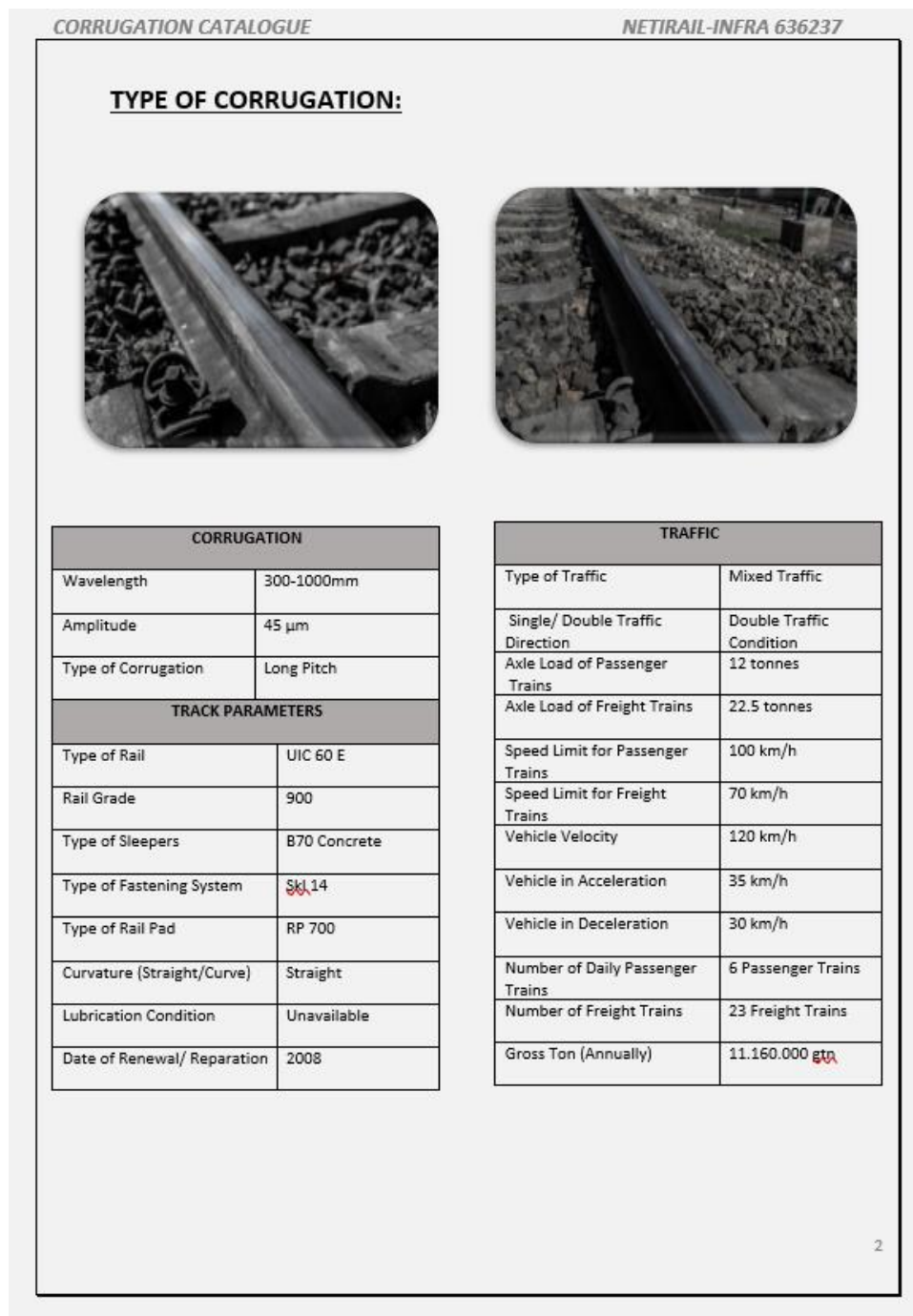


Figure 2.2.3 An example of TCDD corrugation catalogue (long pitch corrugation)

## 2.3 Conclusion and further recommendations



Roger 800 recording car data between 2015 and 2018 were taken and examined. The obtained data was at three month intervals, that also represent the inspection routine of TCDD. After long discussions and also conversations with regional directories, the responsible team selected a few regions to validate the existing Roger 800 data. However, during site visits, it was clarified that, in most cases, the exact locations of the corrugated rails could not be determined. The reason of this is Roger 800 data was directed to wrong coordinates (as line km) because of wheel-skidding. Other reasons to given that invalidate the data could arise from the environmental conditions that measurement performed under, and the mismanagement of equipment integrated on its body.

Despite the errors originating from Roger 800, other reasons are “renewal” of track and/or “repair” (grinding) of the corrugated rails without taking necessary permissions from headquarters or responsible managers. Therefore, it was quite difficult to find the corrugated rails locations’ and then to determine the existing corrugation types. Although the maintenance has usually been implemented in most regions according to the determined schedule, it is observed that the maintenance can be applied at an earlier date (as months). Most of the maintenance activities in TCDD have been implemented based on past experience of the maintenance personnel.

The findings during site visits are given as a catalogue represented in Annex I. As seen in Annex I, renewal/ reparation date of lines having corrugated rails are close to each other. For instance, the earliest one is in 2008. Depending on brief summary about how the corrugation forms, defined in Chapter 1, Section 1.1., the defined years in the corrugation catalogue are quite new, while deformations, such as the corrugation, can be observed over long-time periods. In a conclusion despite these challenges that originated from the current maintenance activities, Annex I was developed, and the responsible team put in their best efforts to complete the task as much as possible by giving the correct and valuable information to the project partners.

Besides the development stage of the corrugation catalogue, it is again necessary to highlight that the form of corrugation depends on several parameters such fastening system types, a number of passing trains, an annual gross ton that pressured the track and weather condition etc as mentioned in previous sections. Hence, it is very difficult to estimate the dominate parameter(s) for each corrugation type without modelling or performing detailed analysis of the related line parts. However, based on Annex I, we can say there is an observable difference related to the annual gross tonnage that the track endured during a certain period where the rail type, grade and fastening system types remain the same. While annual gross tonnage values are increasing, the type of corrugation becomes “long pitch” and mostly it can be seen with naked eyes. On the other hand, the shape of the corrugation points, and distance from each other can change according to track situation which are highly affected by weather conditions and fastening current situation. For medium and short pitch corrugation, because their wavelength is close to each other, it is hard to separate them with naked-eye. Indeed, depending on Roger 800 data and the experience of the regional maintenance personnel, we were able to find few places which have medium and short pitch corrugation.

## 3 Test in Turkey

### 3.1 Brief introduction to test site

The test site selection was performed considering the latest data which were taken from the Roger 800 measurement train, which belongs to TCDD, for the years 2015 and 2018 which provide a basis for the observations. The obtained data from the measurement train was examined very carefully and a few candidate sites are selected for the corrugation test. During the selection of the test sites, the following criteria are taken into account for lines, which are:

- Reachability (how easy is it to access)
- Safety
- Existing power supply
- Existing storage area or place to protect the equipment
- TCDD maintenance and renewal calendar (availability)
- TCDD workers calendar (essential to change the fastening systems)
- Number of the workers can be assigned by regional directorate
- Obtaining permission from TCDD headquarter and also regional directorates
- 3G mobile connection
- Enough space to monitor the trains and taking live data

After long analysis and debates on few candidate test sites characteristics', we decided to perform the test on the Eskişehir- Kütahya- Afyon line which meets the conditions given above. The general overview of the line characteristics is given in Table 3.1.1.

**Table 3.1.1. The selected line general specifications**

Descriptions / Parameters	Explanations / Values
Traffic Type	Mixed (passenger & freight)
Number of Passenger Trains	12
Number of Freight Trains	21
Average Speed	~ 75 km/h
Design Axle Load	≤ 22.5 tons
Steep Grade	0.1 %
Length of the Demo Test	180 m
Daily Gross Rail Load	38,500 gross ton
Rail Type	UIC 60
Travers	Concrete B70
Is the line electrified?	Yes
Existing fastening system	System W14

Eskişehir- Kütahya- Afyon line type is a conventional one. The exact test location is determined as 17+800 km near to Kızılınler, very close to Eskişehir. A photo and open railway map picture of test site are given in Figure 3.1.1 and Figure 3.1.2. respectively.



Figure 3.1.1 Selected test site (Eskişehir- Afyon- Kütahya Line)

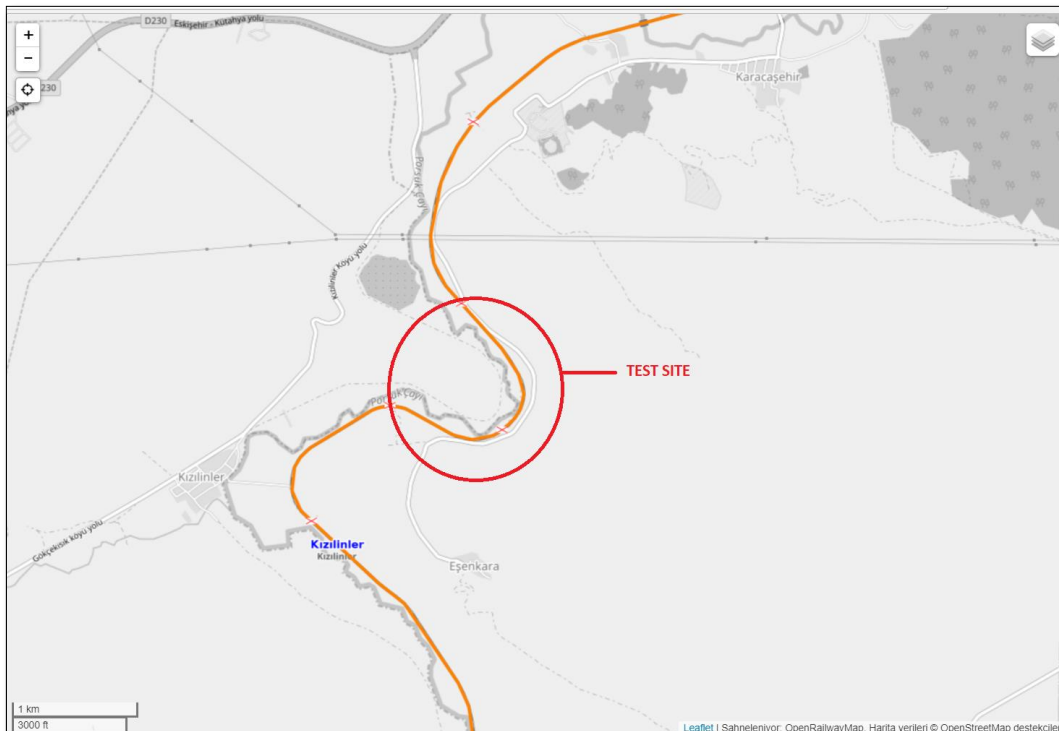


Figure 3.1.2 Demonstration of the selected test site on open railway map

Although the line is continuously electrified unless there are short interruptions in the region, it is noticed that diesel locomotives also used this line. The line is single track, and the traffic type is observed as mixed as stated in Table 3.1.1. Line traffic includes both passenger and freight lines, but TCDD has usually used this line to carry heavy hauls. In other words, the line is dominated by freight trains and in most cases, the line is preferred to carry fuel tanks and various type of cars.

The test site is determined as 180 m long in a plain line that connects two curves. The unscaled representation of the test site is shown in Figure 3.1.3. The first curve on Eskişehir line has a radius of 298 m, the second curve on Kütahya line is 300 m.

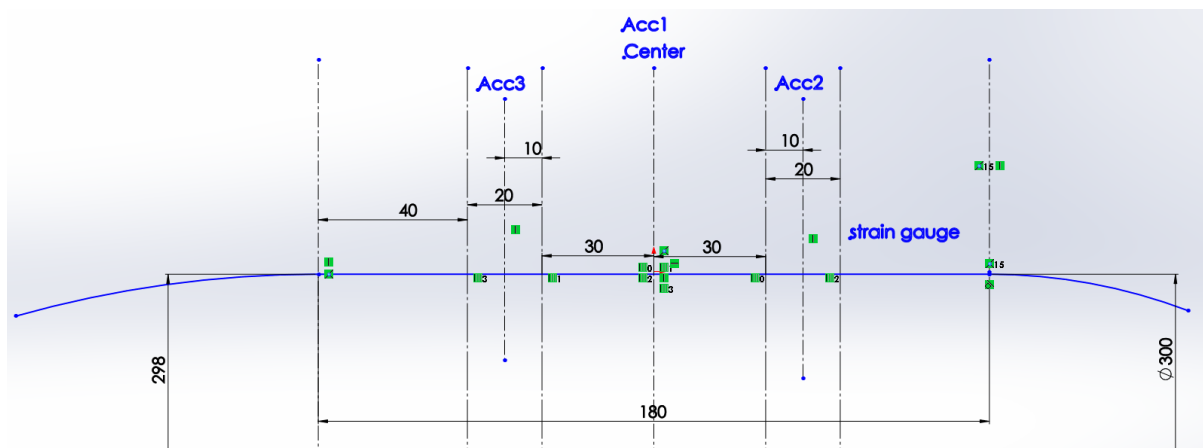


Figure 3.1.3 Unscaled representation of the test line

As mentioned before, the line is electrified, however, the nearest voltage supply to connect the test equipment is the signal cabinet for the passing trains and it is 900 m away from the test site as demonstrated in Figure 3.1.4. To clarify, a photo taken by the existing signalization cabinet, as origin point is given ,in Figure 3.1.5, to understand the distance between the test location and the cabinet. Because of the long distance, to provide power to our equipment, we had to lay almost 1 km cable. The laid cable was spanned to the data logger cabinet with a IP 65 junction box. Since signalization has a vital importance for TCDD to enable the continuity of the transportation, with the connected cable, we were able to provide 10 hours uninterruptable power for our equipment. However, during the first trial of the test, we could not get any alive data because of low quality of Wi-fi connection. The reason is the test site was located in a rural area where the mountains are enclosed so that the 3G signal is rather low comparing to outskirts of Eskişehir. Another important issue is the distance between the power supply and the test location is really far and the laid cable was exposed to the environment. Any extreme change in weather, animal contact (gnawing animals or wild animals) or person contact (workers of TCDD or unknown persons) has a high possibility to interrupt the system. Unfortunately, because the test designed as its nature as a not closed system, we had to take these risks during the test.



Figure 3.1.4 The signalization cabinet used for supplying electricity (220 V) to the test equipment

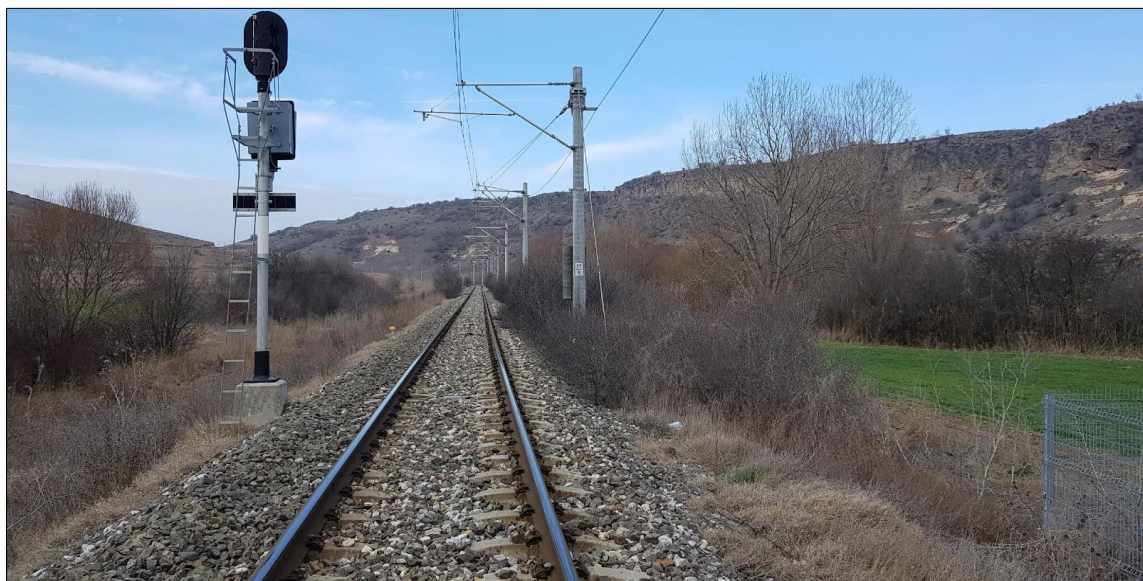


Figure 3.1.5 The photo by taking the signalization cabinet as an origin

Eskişehir is located in the Central Anatolia Region of Turkey and its climate type is “cold semi-arid climate (Bsk)” according to Köppen- Geiger Classification [1]. The annual average temperature was measured as 10.9°C from 1927 to 2017. The coldest month is January where the average temperature is near -2°C. The frost and snowy days usually happen in the winter season, so the temperature can decrease to approximately -25°C in the rural area. However, depending on the climate season (dry or wet), the average temperature can be in the range between 10°C to 15°C. During the spring season, the temperature usually raises above 20°C. The hottest days are in summer season as expected. The average temperature in summer seasons was 27.9°C. The temperature in summer season can raise to 40°C [2].

The significant feature of Eskişehir climate is the temperature variation of day and night is quite large. This variation can reach to 12°C for a day [3]. In autumn season, the temperature decreases below 20 °C and in September, the temperature can drop to near to 0°C [3].

The precipitation in Eskişehir can be seen as snow and heavy rain falls. After December, the precipitation turns to snow until near to April, it gains its form as a rain again. The annual precipitation in Eskişehir was measured as 378.9 kg/m<sup>3</sup>.

During the validation of the test, the temperature graphs of the Eskişehir was given in Figure 3.1.6. The temperature of test site differs form -10°C to 40°C, with heavy rain and snow.



Figure 3.1.6 Temperature values during the validation of the test site [4]

### 3.2 Selection of the test equipment and integration process

The equipment was selected according to the line and test location specifications. The crucial point here is to enable the congruity of each equipment and to establish a working system which can continuously collect data from the site. Thereof, our criteria for selection of equipment are:

- Find a suitable equipment for defined ranges such as choose accelerometer as 16 g or  $\pm 5$  g
- Congruity of the equipment with each other (integration of them)
- Delivery time and guarantee of the supplier (in case of getting broken/defected ones)
- Obtaining different types of fastening systems (most of the companies do not sell them in small amounts)
- The power consumption of equipment

Apart from these criteria, it was difficult to find companies who can provide the test equipment according to PRAG rules because few companies can available to understand the negotiation process and able to provide products that originated in Europe countries. The supply procedure was performed within our budget depending on **PRAG rules: Chapter 2, sub- section 2.4.8 – Negotiated procedure / single tender procedure** [5].

The equipment used for the corrugation tests are explained in below. A few examples of the equipment are given in Figure 3.2.1 and Figure 3.2.2.

- **Sensors & Accelerometer**

A total of six (6) mems-based sensors were used and they were integrated to a data logger sampling at 8 kHz. The Adxl 326 sensor has a frequency response range of 1.6 kHz for 2 axis and 550 Hz for the third axis. The third axis could not be use because of its low frequency value. Sensors were mounted to the glass fiber board by application of the epoxy and then fiber board was stick on the rail again by using epoxy. The reason to use epoxy is according to internal regulations of TCDD, it is forbidden to use any material will create any damage and perforate the rail and tracks components, thereof, we had to apply the epoxy and board as a kind of interface that will have minimum effect on the collected data.

The accelerometers were mounted 20 m away from each other and they integrated into both right and left rails. The integration locations on the rail were the web and foot of the rail. The accelerometers can take z direction (gravity axis) data and the lateral direction (which is perpendicular to the train direction) data.

Different from the applications on the rail, two laser sensors were used to measure the speed of the train. A PLC (Programmable Logic Controller) is used to measure the time difference between the first trigger and second trigger with a sensitivity of 1 millisecond. The taken data is sent to PLC via 0-10 V analogue channel. For example, for voltage at 0 km/hr was measured as 0 (zero) where the voltage for 108 km/hour was measured as 10 V. This speed data was used to be a kind of

trigger mechanism to validate if the sensors were working efficiently. It is necessary to highlight in here that because the nature of the test is open to the environment, the animals (gnawing and wild) may trigger the sensors although rolling stocks are not passing through the line. In the examination of the data, this segregation was performed while cleaning and normalizing the obtained data.

- **Data logger**

One high speed data logger was used for the recording the data coming from the vibration sensors. On the other hand, two low speed data loggers were used to store the speed and strain data. However, during tests including the validation period, the high speed data logger hard disk was burned because of the weather conditions and a blackout in the power supply. In most cases, maintenance personnel can shut down the system due to TCDD security reasons. Therefore, during the test, because of the location in the rural area and low 3G connection, we could not detect the power cut in the system and the weather conditions where close to below zero degrees. Hence, when we performed our regular checks of the system during a site visit, we observed that some of the data taken was lost because of this problem.

Quick action was taken by team site manager and the broken data logger was replaced with a new one, the new version had flexibility to endure harsh weather conditions. In addition, TCDD maintenance personnel was informed again from regional directorate so that we were able to sustain the data processing duration. In addition to these measures to handle control of data loggers for preventing data loss, we replaced a 3G module for the local connection and inform the authorities. The local connection was provided between a data logger for speed and mobile phone (with 3G) that was used as a wi-fi hotspot. The mobile phone can be reached from the remote access with an android application or, vice versa, the mobile phone having the android application can be controlled remotely accessing one of the data loggers net interfaces. Remote access was only able to be provided by one data logger because of the low quality of wi-fi connection (low signal of gsm) in the test site. Through the remote access, the functions of the data logger and momentary recordings can be seen and also the settings of the data logger can be changed.

- **Strain gauges**

The two strain gauges are used to calculate the axle load and they are placed on the right and left foot of the rail. Strain gauges were connected in the form of Wheatstone bridge to minimize temperature effects. 350-ohm strain gauges were used with 5-volt supply to reduce the heating.

- **Cables and connectors**



As mentioned in previously, 900 m cable was laid to supply the power to test equipment. For this cable, attachments (add-in) had to be performed because of the long distance. Apart from this, only connection cables belonging to each equipment and connectors (for data loggers) were used.

▪ **Power supply unit**

The only power supply near to test site is in signalization cabinet which belongs to TCDD. We examined the option to use a diesel generator at the test site, however, there is no place to keep it safe and provide its working continuity. A diesel generator can provide power for 8-9 hours without giving any blackout, but a continuous power supply was needed so that a connection from the signalization cabinet seemed to be the best solution. According to TCDD internal regulations, without obtaining permission, nobody can enter and use the power. Hence, we obtained permission before the implementation phase of the test, unfortunately, the maintenance personnel were not informed about our test so without informing us, they had to cut the power for the security reasons.

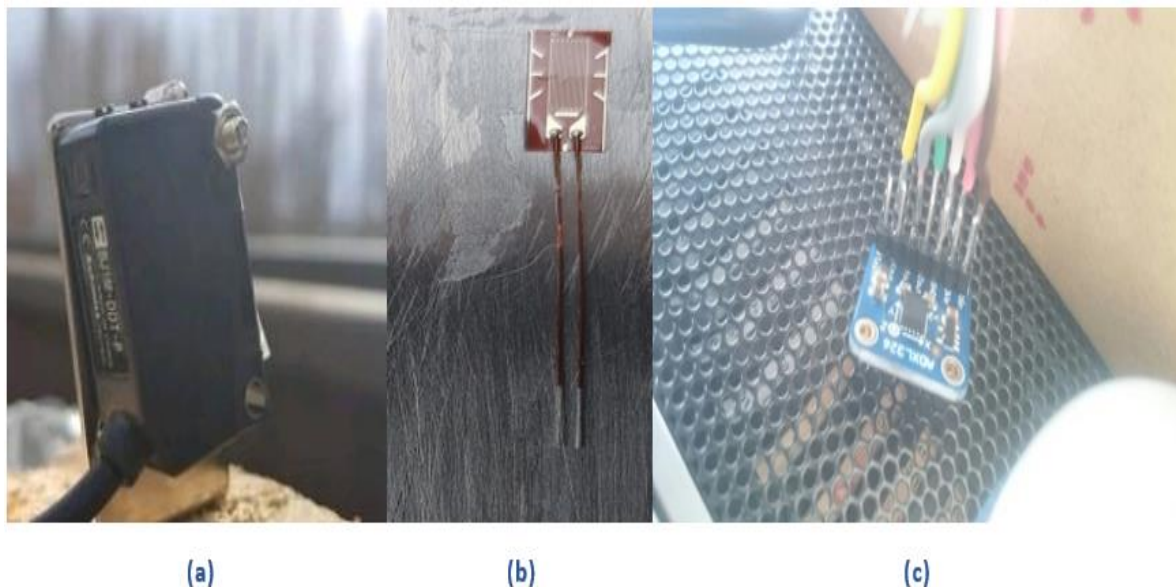


Figure 3.2.1. (a) Laser sensor for speed calculation; (b) Strain gauge (before commissioning); (c) ADXL326 Mems based accelerometer

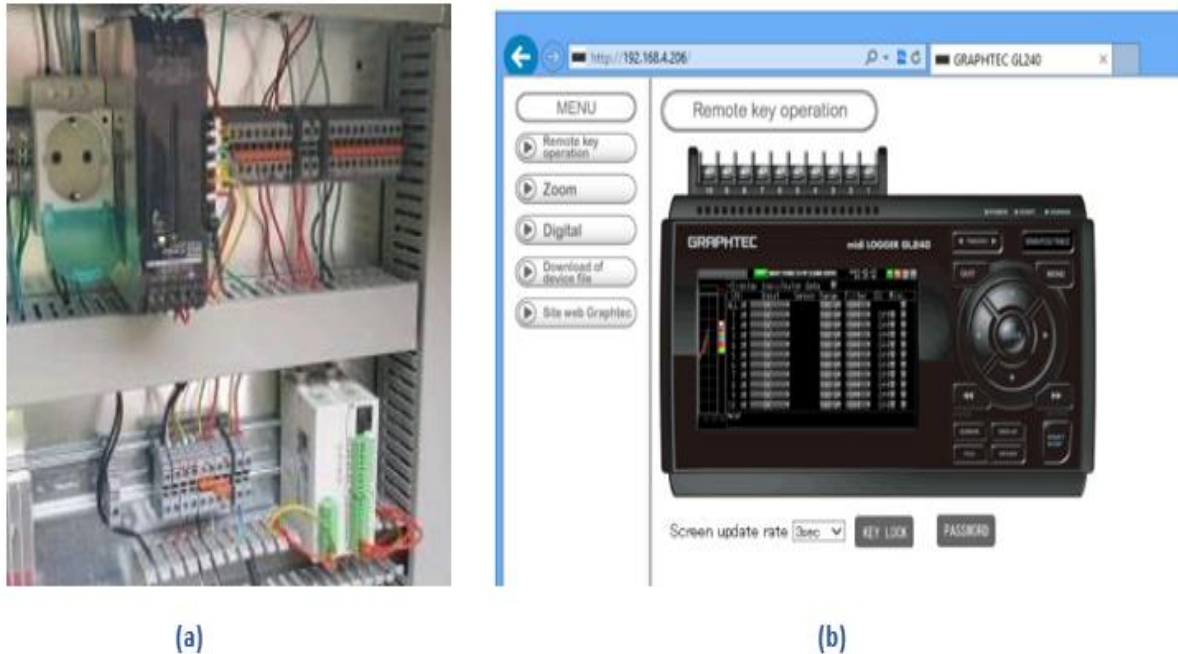


Figure 3.2.2. (a) Integration of the equipment in a board; (b) Demonstration of remote access to the data logger

▪ **Tested fastening components**

For this test, three types of plastic pads are tested in 180m plain line. Their specific features are explained in Table 3.2.1. The selected fastening systems details are given in Figure 3.2.3, Figure 3.2.4 and Figure 3.2.5.

The components of a selected fastening system are:

- Tension clamp
- Angle guide plate
- Rail screw with washer
- Elastic rail pad
- Dowel

The static stiffness of a pad has an important role to dissipate the force applied on the rail to the ballast section. W14 series have a medium static stiffness that is the preference of TCDD without differentiating line specifications. In other words, the current system in TCDD is W14. On the other hand, W21 and HH were chosen to measure their impacts for TCDD lines and form a comparison platform for W14. Although the static stiffness of W21 and W14 seems to be closer to each other

according to given values, HH static stiffness value is rather in extreme range which is equal or greater than 300 kN. It is essential to remind the reader that the authors could not find any analysis or study that compare different type of fastening systems for TCDD.

**Table 3.2.1. The selected fastening system components and plastic pads features**

Parameters	W14	W21	HH
<b>Track Application</b>	High speed and conventional	High speed and conventional	Heavy haul
<b>Speed</b>	High speed $\geq 250$ km/h Conventional $\leq 250$ km/h	High speed $\geq 250$ km/h Conventional $\leq 250$ km/h	$\geq 180$ km/h
<b>Design Axle Load</b>	$\leq 26$ tons	$\leq 26$ tons	$\leq 35$ tons
<b>Curve Radius</b>	High speed $\geq 400$ m Conventional $\leq 150$ m	High speed $\geq 400$ m Conventional $\leq 150$ m	$\geq 400$ m
<b>Vertical Fatigue Strength</b>	2 mm	2.5 mm	1.8mm
<b>Toe Load</b>	9 kN	10 kN	12 kN
<b>Height Adjustment</b>	Optional	Optional	Optional
<b>Gauge Adjustment</b>	$\pm 10$ mm	$\pm 10$ mm	$\pm 10$ mm
<b>Static Stiffness of Rail Pad</b>	60 kN/mm high speed lines	$\geq 40$ kN/mm high speed lines	$\geq 300$ kN/mm heavy haul lines
<b>Electrical Resistance</b>	$\geq 5$ k $\Omega$	$\geq 5$ k $\Omega$	$\geq 5$ k $\Omega$
<b>Rail Creep Resistance</b>	$\geq 9$ kN	$\geq 9$ kN	$\geq 9$ kN

**Tension Clamp - Skl 14**



Tension Clamp which is made from high quality spring steel, transfers the load from the track to the concrete sleeper through its spring arms. It prevents the rail screw from loosening by its elastic structure. Furthermore, it provides up to 2 mm of elasticity under loading.

**Elastic Rail Pad - RP 700**

The rail pad gives elasticity to the system and it resists the vertical loads. Furthermore, its electrically insulating the rail and attenuate noise and vibration where necessary.

W14 Rail Fastening System has various rail pad types;

- TPE
- TPU, PU
- EVA
- EPDM



**Angle Guide Plate - AGP 14 k12**

Angle Guide Plate that is made from high quality polyamide material, connects the rail screw to the sleeper. It is plastic based composition and serves high isolation for track systems.



**Dowel - DWL 25**

Dowel which is made from high quality PA6 material, connects the rail screw to the sleeper. Since it is plastic based composition, it serves as a perfect isolation material for track system.



**Rail Screw with Washer Ss 35 with Uls 7**

Rail Screw connects the tension clamp to the sleeper and the ground. It is made from high quality steel, approved by local and international railway organizations.

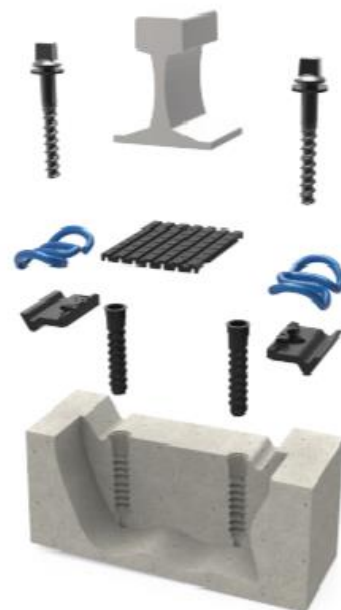


Figure 3.2.3. W14 for high speed and conventional lines

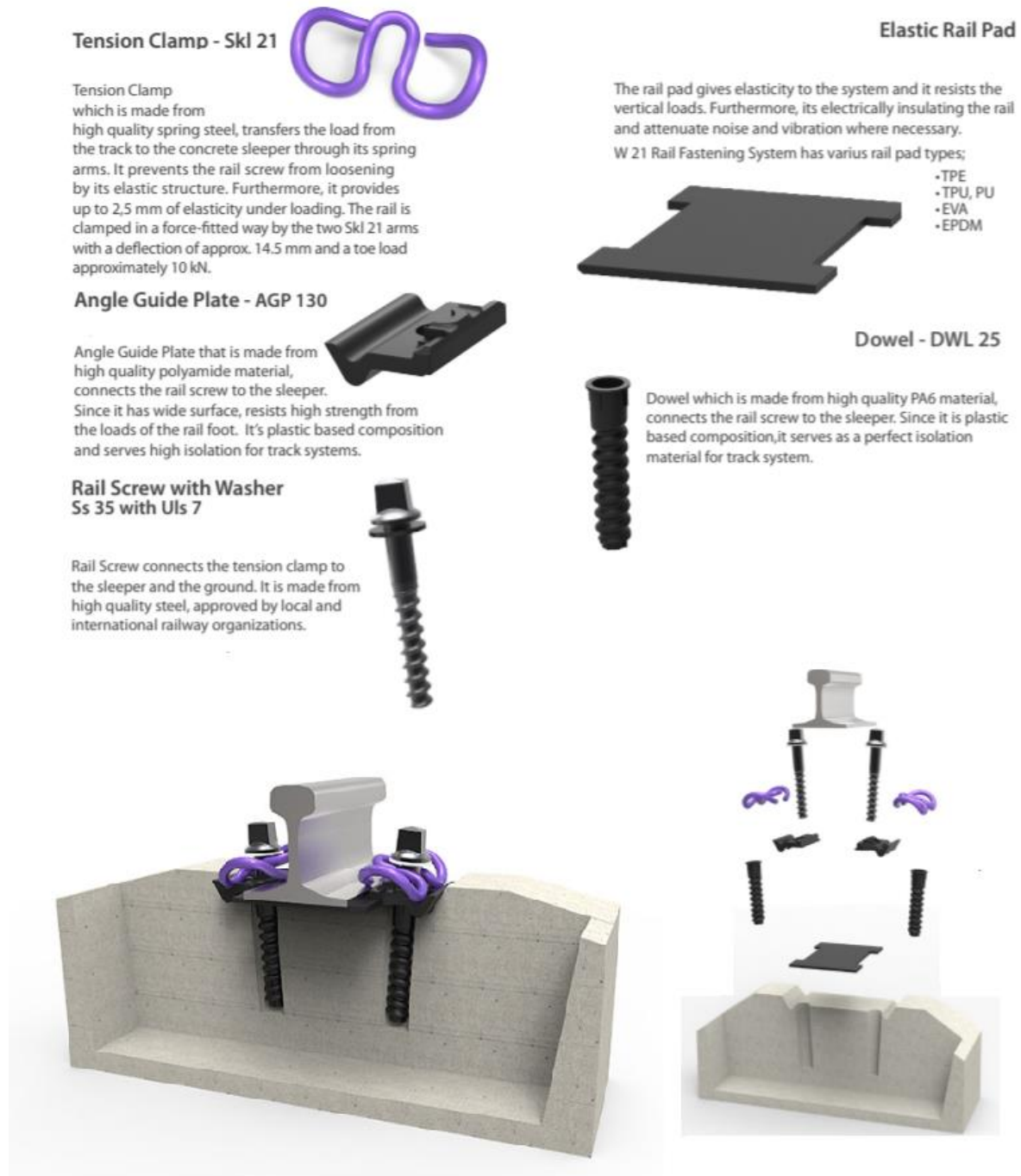


Figure 3.2.4. W21 for high speed and conventional lines

**Tension Clamp - Skl HH**



Tension Clamp which is made from high quality spring steel, transfers the load from the track to the concrete sleeper through its spring arms. It prevents the rail screw from loosening by its elastic structure. Furthermore, it provides up to 1,8 mm of elasticity under heavy load.

**Angle Guide Plate - AGP 130**



Angle Guide Plate that is made from high quality polyamide material, connects the rail screw to the sleeper. It's wide rail surface, resists high strength from the loads of the rail foot. It's plastic based composition serves high isolation for track systems.

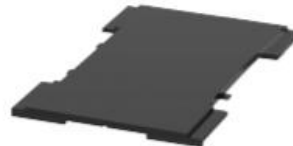
**Rail Screw with Washer Ss 35 with Uls 7**



Rail Screw connects the tension clamp to the sleeper and the ground. It is made from high quality steel, approved by local and international railway organizations.

**Elastic Rail Pad - RP 900**

The rail pad gives elasticity to the system and it resists the vertical loads. Furthermore, its electrically insulating the rail and attenuate noise and vibration where necessary. HH System can be used with various rail pad types;



- TPE
- TPU
- PU

**Dowel - DWL 25**



Dowel which is made from high quality PA6 material, connects the rail screw to the sleeper. Since it is plastic based composition, it serves as a perfect isolation material for track system.

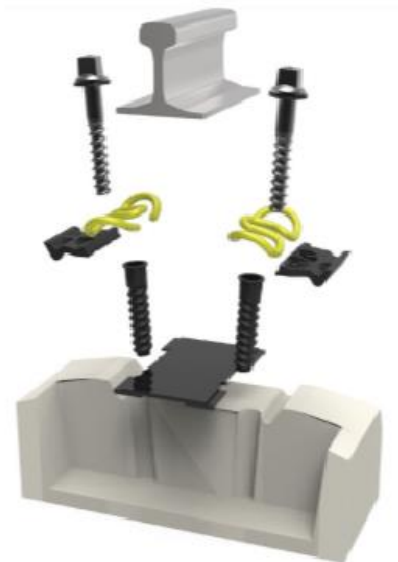
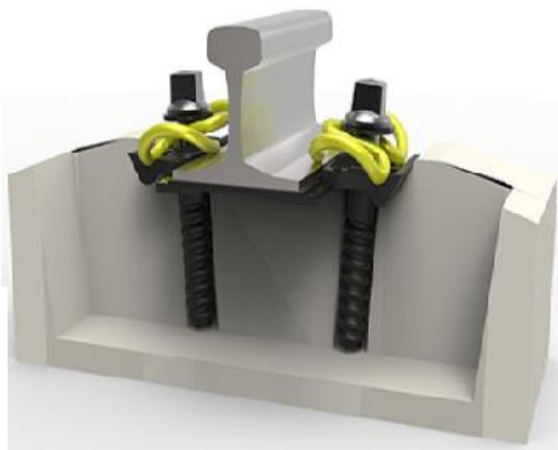


Figure 3.2.5. W21 for heavy haul system for freight and cargo trains

### 3.3 Methodology

To obtain a vibration analysis data were recorded with 8 kHz frequency. The sensors used have 1.6 kHz response range. These recordings were used to plot acceleration amplitude and time graphs. To analyse the dominant frequencies, Fast Fourier Transform (FFT) was applied. These dominant frequencies are important to compare the theoretical results and test results.

To give a brief information about the FFT was derived from Fourier Series. The formulas of Fourier Transform (FT) are given in Equation (I) and Equation (II). Fourier transform maps a time series such as audio samples into the series of frequencies (amplitudes and phases) that composed the time series.

**Forward Fourier Transform:**  $F(k) = \int_{-\infty}^{\infty} f(x)e^{-2\pi ikx} dk$  Equation (I)

**Inverse Fourier Transform :**  $F(k) = \int_{-\infty}^{\infty} f(x)e^{2\pi ikx} dk$  Equation (II)

where  $f$  is the frequency and  $n=1,2,3\dots$  and  $k$  is the time [6].

It is necessary to note that  $e^{xi} = \cos(x) + i \sin(x)$ . Additionally, Fast Fourier Transform (FFT) takes  $O(n \log(n))$  for time [6].

The sampling theorem (Nyquist-Shannon Theory) claims that a signal should be sampled at least twice as fast as the bandwidth of the signal to reconstruct the waveform [7]. In other words, sampling frequency should be at least twice of the maximum frequency as stated in Equation (III).

**Nyquist sampling rate :**  $f_s > 2 f_{\max}$  Equation (III)

$2f_{\max}$  is called the Nyquist sampling rate and sometimes  $f_{\max}$  called as Nyquist frequency [7].

Based on this theorem, 8 kHz sampling frequency was chosen during the test. The method that we followed is given as given in below by logical order.

- 1<sup>st</sup> phase: Examination of the data during the passing time of the train
- 2<sup>nd</sup> phase: Identifying the maximum data of the 1<sup>st</sup> phase.
- 3<sup>rd</sup> phase: Analyse 500 millisecond data (4000 data points) before and after of the maximum data determined in 2<sup>nd</sup> phase
- 4<sup>th</sup> phase: Apply the FFT to these collected data (as a total 8000 data points in one second)

### 3.4 Test results

#### 3.4.1 For passenger trains

First of all, during the test, the obtained data was cleaned to see the test result in a clearer way. Therefore, unrelated data, inconsistent data was disregarded. Checking the passenger trains passing time schedule obtained from TCDD, the passenger trains were identified with the validation of TCDD experts. Additionally, the trains with similar speed and axle loads were observed to eliminate to prevent unsuitable data formation (nullified data mostly). Passenger trains typically have a speed of

20 m/s (70 km/h), however, depending on the driver behaviour, this speed limit (usually taken as an average) may be exceeded time to time. To identify this problem, two laser sensor measures the speed were put before taking the data and the speed and train type were validated by using the data coming from both laser sensors.

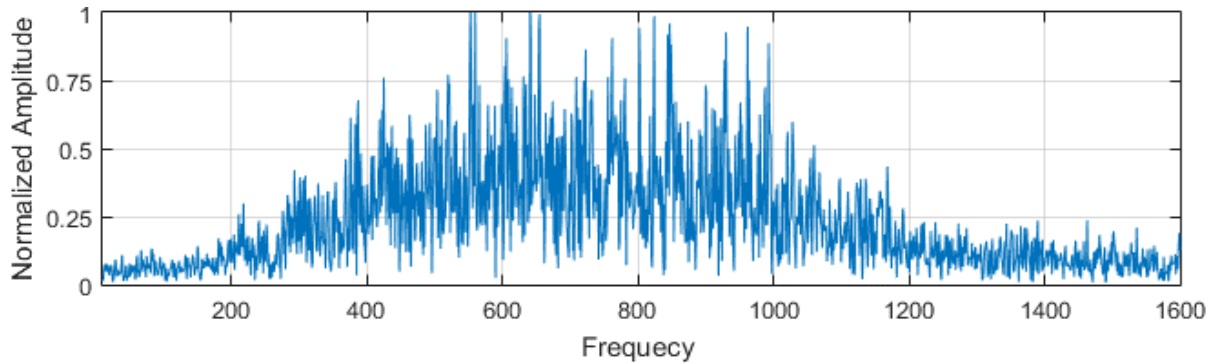


Figure 3.4.1.1. W14 fastening system results for passenger trains

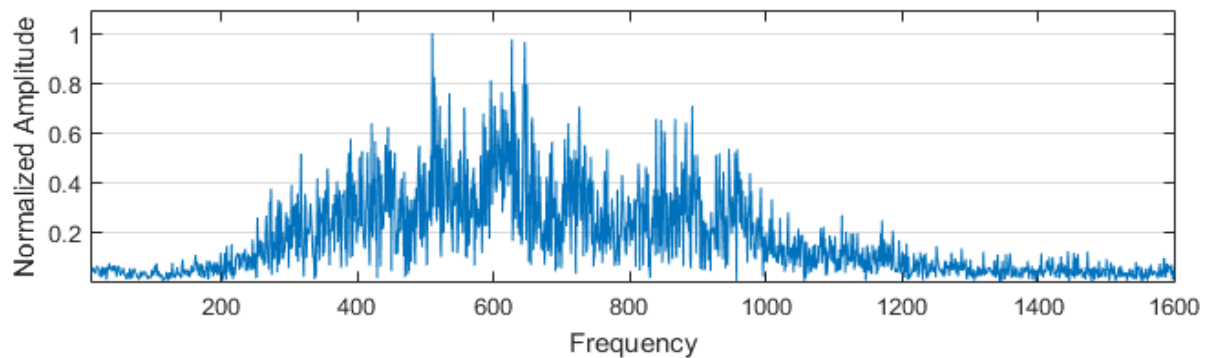


Figure 3.4.1.2. W21 fastening system results for passenger trains

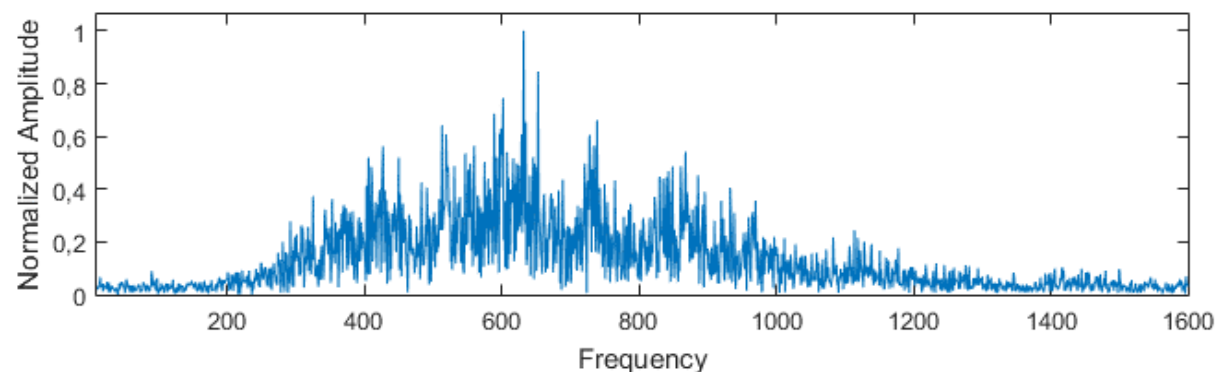


Figure 3.4.1.3. HH fastening system results for passenger trains



During all calculations performed for the passenger trains, the speed was taken as 70 km/hour with  $\pm 10\%$  error margin. Axle loads for all passenger trains were similar at 18 tonnes, to be specific, the maximum difference measures as 18 tonnes with  $\pm 10\%$  error margin. The predominant frequencies measured are given below. The predominant zone was estimated according to expert judgement, it can be said that between 500 Hz and 650 Hz were slightly dominant compared to others.

- In channel 1 predominant frequencies were between 600 Hz and 1000 Hz
- In channel 2 predominant frequencies were between 600 Hz and 750 Hz
- In channel 3 frequencies were evenly spread through the spectrum range

The passenger trains acceleration time graphs were compared. The type of the trains passing through the test site was identified by checking the similarities of parameters given below. During processing the data and finding the similarities, by also controlling the passing time of the trains taken from TCDD, the best possible matches were identified by validating through TCDD experts.

- Similar axle loads
- Similar speed
- Similar axle type and distance
- Similar traction sets (electrified)
- Similar train configuration

However, some parameters could not be matched: Time effects (including degradation in rails and weather conditions on tracks: elasticity of pads and variation of temperature effect on the sensors).

As mentioned earlier, HH type has the highest static stiffness ( $\geq 300$  kN/mm), W14 has the moderate static stiffens (60 kN/mm) and finally, W21 has the lowest static stiffness ( $\geq 40$  kN/mm). In Figure 3.4.1.4., to be able to compare these plastic pads, the plotted graph was normalized. The results showed that HH has the lowest damping because of the higher stiffness values it has. On the other hand, W14 has a better damping and few local high peaks. When it comes to W21, its behaviour was closer to W14 ones. It also can be seen that W14 and W21 have a uniformity over the whole graph given as in Figure 3.4.1.5. Additionally, the main amplitudes for W14 and W21 are between 500 and 650 Hz.

As a conclusion, W14 and W21 give almost similar results while HH seems to be the most unsuitable pad. It is essential to remember that the test duration is less than one year so that the elasticity of the plastic pads and durability of the fastening components, as well as their impact on the system, could not be observed. It is a fact that these systems are open to the environment and highly affected from the weather conditions that may change their durability, usage time, stiffness value (depending on type) and their connection distance. In addition, although the speed restrictions are identified for TCDD lines during the test, it was observed that sometimes the trains were over the speed limits. Therefore, it is also an unignorable fact that the results may be affected the variations in high speed. Finally, the seasonal effects and speed variation on the fastening system and plastic pads can be another research topic while taking into account the current research.

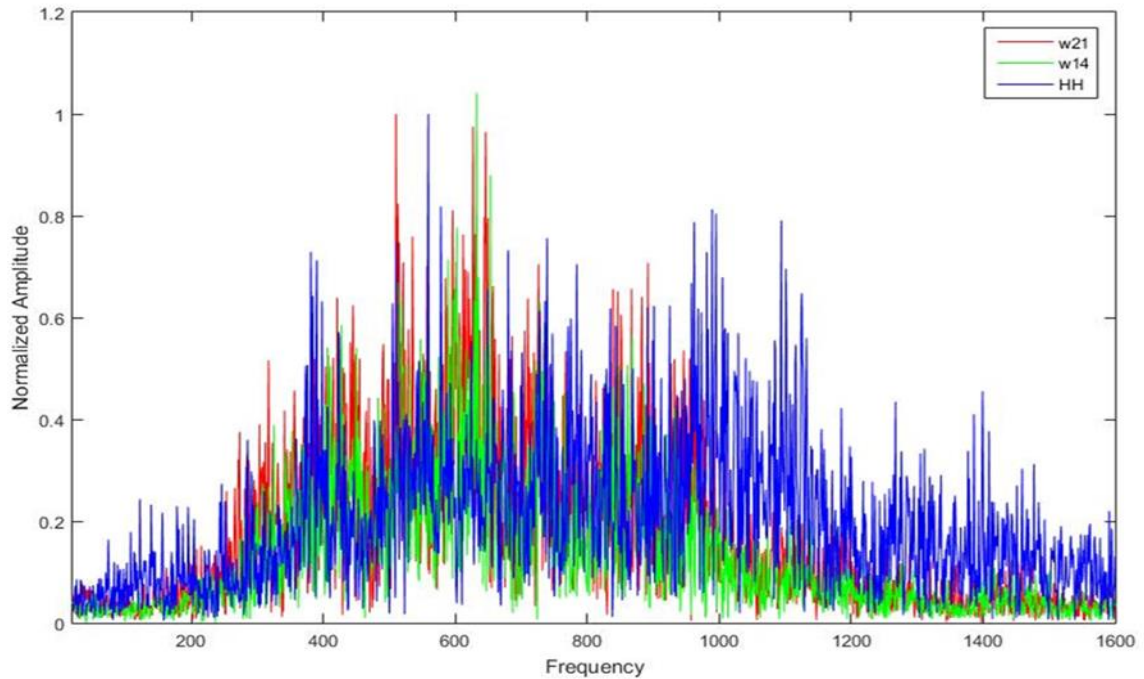


Figure 3.4.1.4. Comparison of fastening systems the results for passenger trains

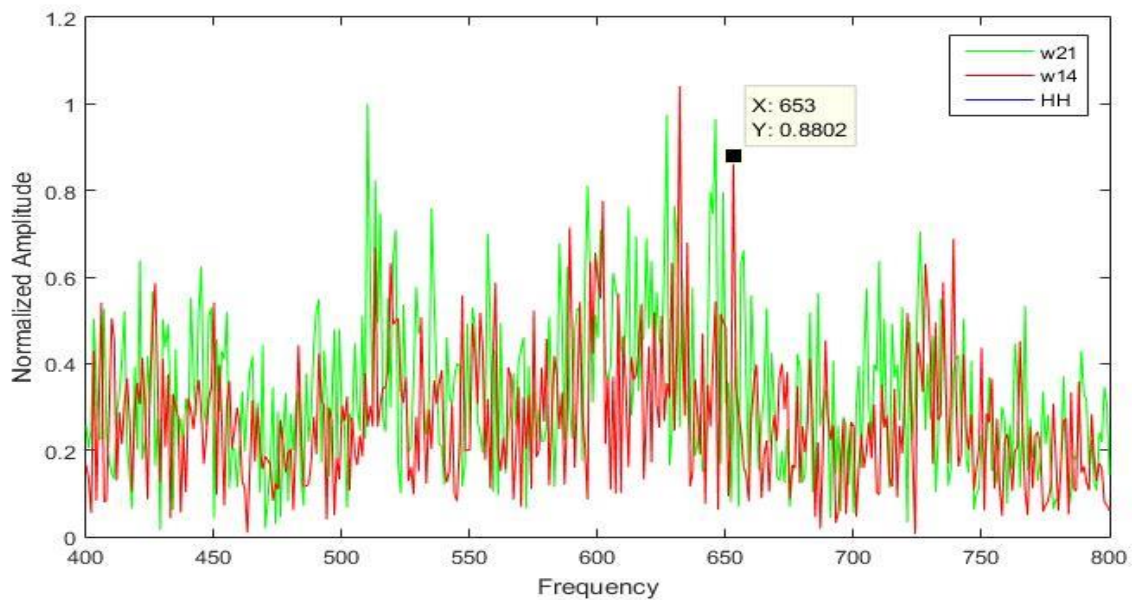


Figure 3.4.1.5. Comparison of W14 and W21 fastening systems for passenger trains

### 3.4.2 For freight trains

The same procedures and assumptions were performed by freight trains. The only difference was axle loads for freight trains were calculated as 20 tonnes. Therefore, the maximum difference for freight trains were 22 tonnes with  $\pm 20\%$  error margin.

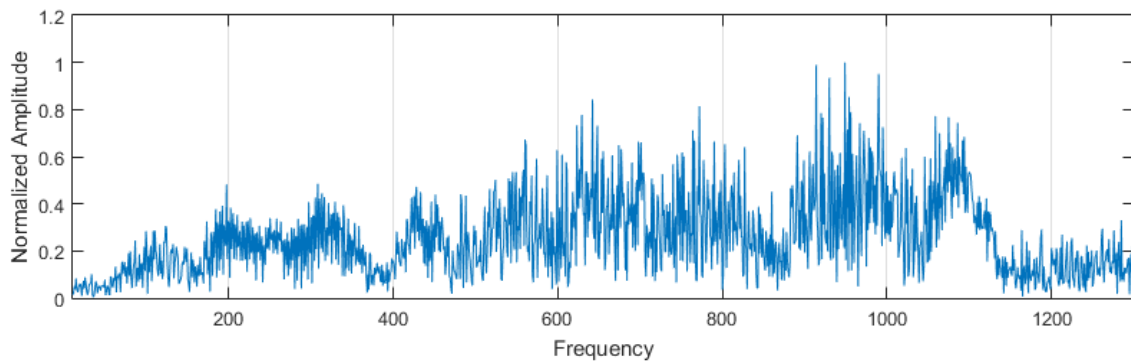


Figure 3.4.2.1. HH fastening system results for freight trains

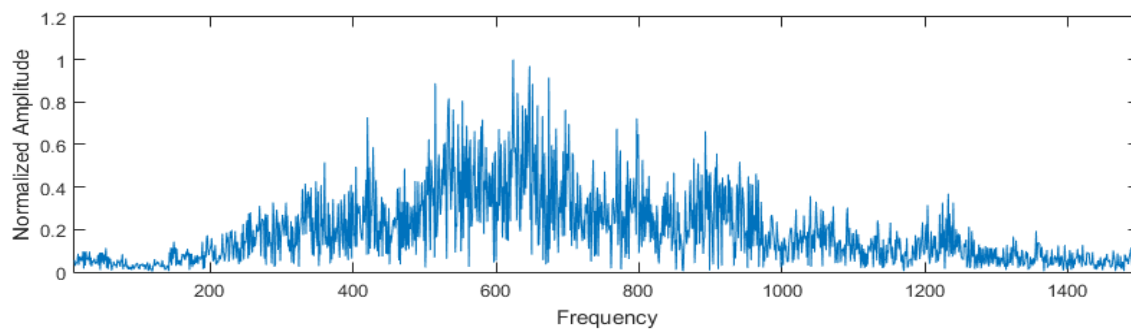


Figure 3.4.2.2. W21 fastening system results for freight trains

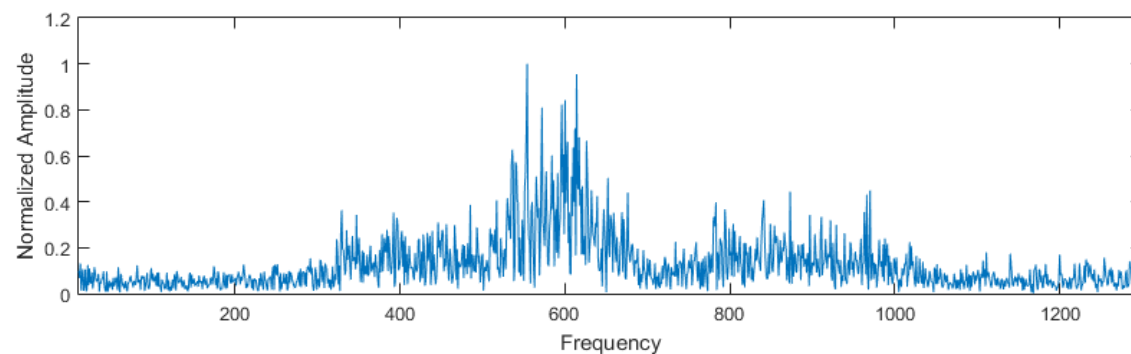


Figure 3.4.2.3. W14 fastening system results for freight trains

All graphs in this section belonged to freight trains that have similar axle load and speeds. The freight trains have four (4) wheels on one bogie as two pairs on the left side and two pairs on the right side. Thereof, acceleration time graphs have two similar symmetrical peaks because of the wheel structure that is different from the passenger trains. To give a specific detail, HH system has higher dominant peaks up to 1000 Hz where the first highest peaks are in the region of 900-1000 Hz and the second highest peaks are in the region of 600-800 Hz. On the other hand, W21 (shown as SKL 21) has dominant frequencies are around 650-750 Hz while W14 (shown as SKL 14) has peaks around 500-650 Hz.

In Figure 3.4.2.4., three systems were combined and demonstrated as one graph to detect the most effective fastening system by normalizing the amplitude. As seen in the figure, HH has the highest frequency rating and it has higher amplitudes over the whole range.

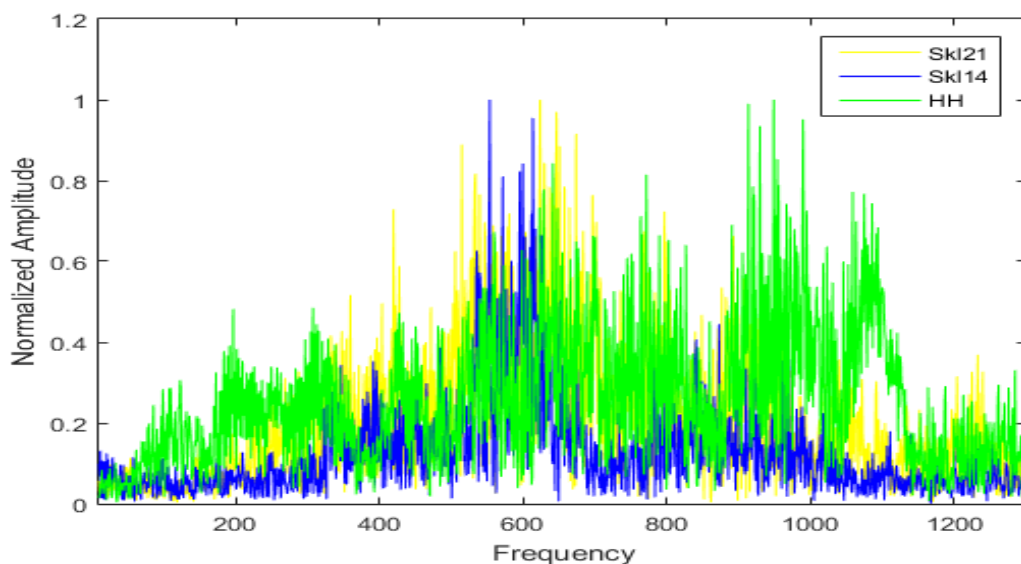


Figure 3.4.2.4. Comparison of fastening systems the results for freight trains

To differentiate the difference between W14 and W21, HH was taken out from the graph. The results for W14 and W21 are demonstrated in Figure 3.4.2.5. According to our results and as well as can be seen from below figure, W14 demonstrated a better performance comparing to W21. On the other hand, W14 has a narrower band contrary to W21 which has a wider frequency range. However, the results of both fastening systems are quite similar to each other.

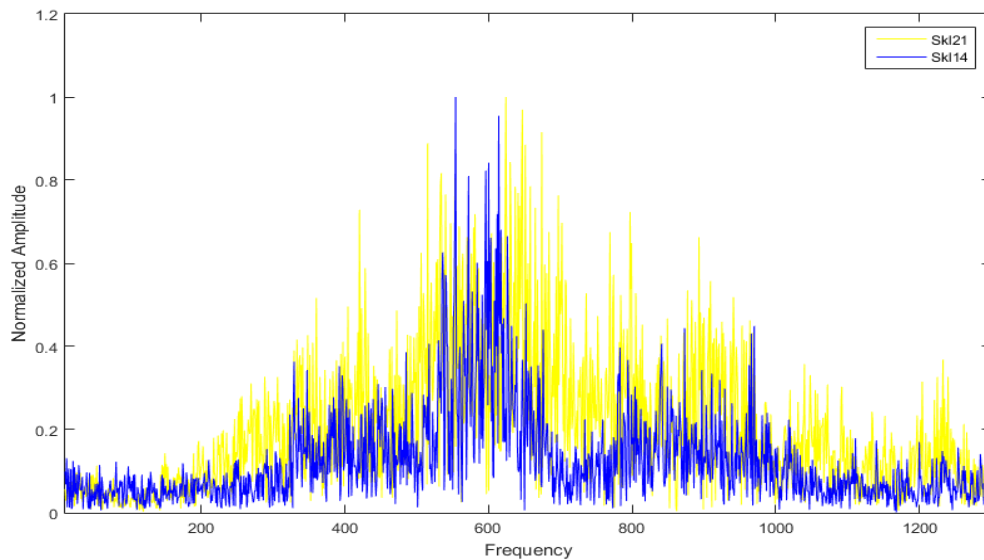


Figure 3.4.2.5. Comparison of W14 and W21 fastening systems for freight trains

### 3.5 Discussion and conclusion

In summary, the frequency behaviours of the fastening systems are very similar. The frequency shift in three fastening systems was observed. Although the shift may have originated from speed variations during the test according to our estimations, the other parameters such as weather impact, slip-stick effect, deformations on the rail and its components etc may have a more dominant effect than the speed variation. To define this exactly, a few tests and modelling/simulation should be performed.

One of the other results of the test is that frequency range is more dominant between 600 Hz and 750 Hz with a speed of 20 m/s. This is also in the ranges that short pitch corrugation effects can be seen. As know when the speed is high, it is expected to have higher frequencies. However, it is not possible to perform the test with high speed because of obligations stated in TCDD internal regulations.

For passenger trains, we have similarities between the tested three fastening systems. HH has a different characteristic from a vibration perspective and with less damping. On the other hand, similarities between W14 and W21 are quite close, but we observed that the current system applied in TCDD systems, W14, has better performance compared to W21.

For freight trains, the peaks are sharper comparing to passenger trains' results. Although the results of these trains are close to the passenger ones, the effect of the fastening system can be more easily observed because of the higher axle loads and double wheel configuration. According to the analysis, again, W14 demonstrated better performance compared to W21.

### 3.5 References

- [1] "Climate Classification of Turkey." [Online]. Available: <https://mgm.gov.tr/iklim/iklim-siniflandirmalari.aspx?m=ESKISEHIR>. [Accessed: 08-May-2018].
- [2] "Meteoroloji Genel Müdürlüğü." [Online]. Available: <https://www.mgm.gov.tr/veridegerlendirme/il-ve-ilceler-istatistik.aspx?k=A&m=ESKISEHIR>. [Accessed: 08-May-2018].
- [3] "Eskisehir İklimsel Bilgiler." [Online]. Available: [http://www.eosb.org.tr/sosyal\\_gostergeler/iklim\\_2.html](http://www.eosb.org.tr/sosyal_gostergeler/iklim_2.html). [Accessed: 08-May-2018].
- [4] AccuWeather, "Eskişehir için Hava Durumu 2018." [Online]. Available: <https://www.accuweather.com/tr/tr/eskisehir/317856/january-weather/317856?monyr=1/1/2018&view=table>. [Accessed: 11-May-2018].
- [5] "PRAG - European Commission - DG International Cooperation and Development." [Online]. Available: <http://ec.europa.eu/europeaid/prag/document.do?nodeNumber=2.4.8&id=>. [Accessed: 02-May-2018].
- [6] M. Handley, "Fourier Transforms." UCL.
- [7] "Nyquist Theorem --Sampling Rate Versus Bandwidth."

## 4 Conclusions

---

In the deliverable, the development of rail short pitch corrugation is examined using a novel modeling approach. Although the enigma remains unsolved, new insights on the phenomenon are described. The approach consists of simulating the vehicle-track dynamic interactions, which are directly and instantaneously coupled through frictional rolling contact. Wear is assumed to be the damage mechanism. The wheel, track and contact are treated in three dimensions so that the structural, geometric and material properties of the system and its components can be modeled sufficiently. The analysis concentrates on the transient rolling at the corrugation and the behavior of the vehicle-track system under the rapid oscillating loading of Dutch railway track and traffic in an effort to identify the preferred conditions under which corrugation can consistently initiate and grow. The findings and insights are summarized as follows.

- 1) Along the longitudinal centerline of the contact patch, increases in the contact area, maximum pressure, shear stress and micro-slips at the corrugation crest are small, and some of them even decrease with increases in the corrugation amplitude. However, changes at the trough are large. The large micro-slip and the significantly reduced contact pressure at the trough are the major contributions to the differential wear, which causes corrugation initiation and growth. The dependence of the normal contact force on corrugation excitation is strong, and the dependence of the longitudinal contact force on excitation is relatively weak.
- 2) In addition to the commonly-accepted hypothesis for corrugation studies, i.e., the vertical vibration modes of the vehicle-track system determine the development of corrugation, it is found that the longitudinal vibration modes are also important. Longitudinal modes are likely to be important for the initiation of corrugation, and when the corrugation amplitude is sufficiently large, the vertical modes will be dominant. For intermediate situations, the longitudinal and vertical modes together determine whether the corrugation will grow or be suppressed by wear depending on whether the wear is of the necessary consistent frequency and phase.
- 3) The main frequencies of the vertical and longitudinal vibration modes and contact forces, as well as the resulting wear are different. Consequently, a condition (that might not be unique) for corrugation to consistently initiate and grow should be that the longitudinal and vertical main frequencies are consistent. This consistency may be achieved by the control of certain track parameters, for instance by properly constraining the rail fastening.

The modeling and findings agree with field observations (Figure 1.1) of the distribution of corrugation with different severities. The proposed modeling is promising for corrugation analyses. Future work may include identifying the track parameters required for the system to converge to the preferred frequencies and wavelengths and investigating the phase-fixing mechanism of wear that promotes

corrugation growth at every wheel passage. To this end, the first focus should be on rail fastening. Previous work has shown that the fastening system, including the rail pads, has a strong influence on the vertical and longitudinal dynamics.

A catalogue for corrugation was described. This catalogue could be taken as guideline for the monitoring of corrugation. The catalogue was formed by taking into account the existing information taken from the headquarter and regional directorates of TCDD. Thereof, a specific photo (as left and right rails), track parameters and traffic situation are described. It divided into three sections: Corrugation, track parameters and traffic. The corrugation classification was made according to wavelength range. The short, medium and long pitch corrugation were defined as 30 mm -100 mm, 100 mm -300 mm and above 300 mm respectively.

Test results were obtained in Turkey for a corrugated rail under different conditions. The test site selection was performed considering the latest data were taken from Roger 800 measurement train which belongs to TCDD for the year 2015 and 2018 which were provided as a base. The obtained data from the measurement train was examined very carefully and a few candidate sites were selected for the corrugation test. After long analysis and debates on few candidate test sites characteristics', the test was decided to perform on Eskişehir- Kütahya- Afyon line. Eskişehir- Kütahya- Afyon line type is a conventional one. Exact test location was determined as 17+800 km near to Kızılınler, very close to Eskişehir. The test site was determined as 180 m long in a plain line that connects two curves. Three types of fastening systems were applied. W14, W21 and HH. In summary, the frequency behaviours of the fastening systems were considerably similar. The analysis was made both passenger and freight trains. For the passenger and freight trains, W14 gave better results compared to other fastening systems.



D2.6: Tailoring track to avoid  
corrugations: Traffic dependant  
selection of rail cross-section, clips  
and pads to avoid or delay  
corrugation

---

NeTIRail-INFRA  
H2020-MG-2015-2015  
GA-636237  
2018/05/16

## **Annex I : Corrugation Catalogue**

---

**CORRUGATION CATALOGUE**

**NETIRAIL-INFRA 636237**

**TYPE OF CORRUGATION:**



CORRUGATION	
Wavelength	300-1000mm
Amplitude	55µm
Type of Corrugation	Long Pitch
TRACK PARAMETERS	
Type of Rail	UIC 60 E
Rail Grade	900
Type of Sleepers	B70 Concrete
Type of Fastening System	Skl 14
Type of Rail Pad	RP 700
Curvature (Straight/Curve)	Curve
Lubrication Condition	Unavailable
Date of Renewal/ Reparation	2009

TRAFFIC	
Type of Traffic	Mixed Traffic
Single/ Double Traffic Direction	Double Traffic Condition
Axle Load of Passenger Trains	12 tonnes
Axle Load of Freight Trains	22.5 tonnes
Speed Limit for Passenger Trains	70 km/h
Speed Limit for Freight Trains	70 km/h
Vehicle Velocity	120 km/h
Vehicle in Acceleration	35 km/h
Vehicle in Deceleration	30 km/h
Number of Daily Passenger Trains	12 Passenger Trains
Number of Freight Trains	21 Freight Trains
Gross Ton (Annually)	11.200.000 gtn

**CORRUGATION CATALOGUE**

**NETIRAIL-INFRA 636237**

**TYPE OF CORRUGATION:**



CORRUGATION	
Wavelength	300-1000mm
Amplitude	45 µm
Type of Corrugation	Long Pitch
TRACK PARAMETERS	
Type of Rail	UIC 60 E
Rail Grade	900
Type of Sleepers	B70 Concrete
Type of Fastening System	Skl 14
Type of Rail Pad	RP 700
Curvature (Straight/Curve)	Straight
Lubrication Condition	Unavailable
Date of Renewal/ Reparation	2008

TRAFFIC	
Type of Traffic	Mixed Traffic
Single/ Double Traffic Direction	Double Traffic Condition
Axle Load of Passenger Trains	12 tonnes
Axle Load of Freight Trains	22.5 tonnes
Speed Limit for Passenger Trains	100 km/h
Speed Limit for Freight Trains	70 km/h
Vehicle Velocity	120 km/h
Vehicle in Acceleration	35 km/h
Vehicle in Deceleration	30 km/h
Number of Daily Passenger Trains	6 Passenger Trains
Number of Freight Trains	23 Freight Trains
Gross Ton (Annually)	11.160.000 gtn

**CORRUGATION CATALOGUE**

**NETIRAIL-INFRA 636237**

**TYPE OF CORRUGATION:**



CORRUGATION	
Wavelength	100-300mm
Amplitude	28 µm
Type of Corrugation	Medium Pitch
TRACK PARAMETERS	
Type of Rail	UIC 60 E
Rail Grade	900
Type of Sleepers	B70 Concrete
Type of Fastening System	Skl 14
Type of Rail Pad	RP 700
Curvature (Straight/Curve)	Straight
Lubrication Condition	Unavailable
Date of Renewal/ Reparation	2010

TRAFFIC	
Type of Traffic	Mixed Traffic
Single/ Double Traffic Direction	Double Traffic Condition
Axle Load of Passenger Trains	12 tonnes
Axle Load of Freight Trains	22.5 tonnes
Speed Limit for Passenger Trains	100 km/h
Speed Limit for Freight Trains	70 km/h
Vehicle Velocity	120 km/h
Vehicle in Acceleration	35 km/h
Vehicle in Deceleration	30 km/h
Number of Daily Passenger Trains	8 Passenger Trains
Number of Freight Trains	12 Freight Trains
Gross Ton (Annually)	6.350.000 gtn

**CORRUGATION CATALOGUE**

**NETIRAIL-INFRA 636237**

**TYPE OF CORRUGATION:**



CORRUGATION	
Wavelength	30-100mm
Amplitude	10µm
Type of Corrugation	Short Pitch
TRACK PARAMETERS	
Type of Rail	UIC 60 E
Rail Grade	900
Type of Sleepers	B70 Concrete
Type of Fastening System	Skl 14
Type of Rail Pad	RP 700
Curvature (Straight/Curve)	Straight
Lubrication Condition	Unavailable
Date of Renewal/ Reparation	2012

TRAFFIC	
Type of Traffic	Mixed Traffic
Single/ Double Traffic Direction	Double Traffic Condition
Axle Load of Passenger Trains	12 tonnes
Axle Load of Freight Trains	22.5 tonnes
Speed Limit for Passenger Trains	100 km/h
Speed Limit for Freight Trains	70 km/h
Vehicle Velocity	120 km/h
Vehicle in Acceleration	35 km/h
Vehicle in Deceleration	30 km/h
Number of Daily Passenger Trains	12 Passenger Trains
Number of Freight Trains	6 Freight Trains
Gross Ton (Annually)	4.400.000 gtn

**CORRUGATION CATALOGUE**

**NETIRAIL-INFRA 636237**

**TYPE OF CORRUGATION:**



CORRUGATION	
Wavelength	30-100mm
Amplitude	10µm
Type of Corrugation	Short Pitch
TRACK PARAMETERS	
Type of Rail	UIC 60 E
Rail Grade	900
Type of Sleepers	B70 Concrete
Type of Fastening System	Skl 14
Type of Rail Pad	RP 700
Curvature (Straight/Curve)	Straight
Lubrication Condition	Unavailable
Date of Renewal/ Reparation	2013

TRAFFIC	
Type of Traffic	Mixed Traffic
Single/ Double Traffic Direction	Double Traffic Condition
Axle Load of Passenger Trains	12 tonnes
Axle Load of Freight Trains	22.5 tonnes
Speed Limit for Passenger Trains	100 km/h
Speed Limit for Freight Trains	70 km/h
Vehicle Velocity	120 km/h
Vehicle in Acceleration	35 km/h
Vehicle in Deceleration	30 km/h
Number of Daily Passenger Trains	10 Passenger Trains
Number of Freight Trains	14 Freight Trains
Gross Ton (Annually)	7.700.000 gtn

**CORRUGATION CATALOGUE**

**NETIRAIL-INFRA 636237**

**TYPE OF CORRUGATION:**



CORRUGATION	
Wavelength	100-300mm
Amplitude	25µm
Type of Corrugation	Medium Pitch
TRACK PARAMETERS	
Type of Rail	UIC 60 E
Rail Grade	900
Type of Sleepers	B70 Concrete
Type of Fastening System	Skl 14
Type of Rail Pad	RP 700
Curvature (Straight/Curve)	Straight
Lubrication Condition	Unavailable
Date of Renewal/ Reparation	2008

TRAFFIC	
Type of Traffic	Mixed Traffic
Single/ Double Traffic Direction	Double Traffic Condition
Axle Load of Passenger Trains	12 tonnes
Axle Load of Freight Trains	22.5 tonnes
Speed Limit for Passenger Trains	100 km/h
Speed Limit for Freight Trains	70 km/h
Vehicle Velocity	120 km/h
Vehicle in Acceleration	35 km/h
Vehicle in Deceleration	30 km/h
Number of Daily Passenger Trains	6 Passenger Trains
Number of Freight Trains	8 Freight Trains
Gross Ton (Annually)	4.450.000 gtn

**CORRUGATION CATALOGUE**

**NETIRAIL-INFRA 636237**

**TYPE OF CORRUGATION:**



CORRUGATION	
Wavelength	300-1000mm
Amplitude	70µm
Type of Corrugation	Long Pitch
TRACK PARAMETERS	
Type of Rail	UIC 60 E
Rail Grade	900
Type of Sleepers	B70 Concrete
Type of Fastening System	Skl 14
Type of Rail Pad	RP 700
Curvature (Straight/Curve)	Curve
Lubrication Condition	Unavailable
Date of Renewal/ Reparation	2010

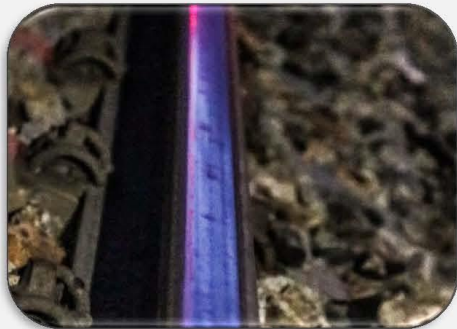
TRAFFIC	
Type of Traffic	Mixed Traffic
Single/ Double Traffic Direction	Double Traffic Condition
Axle Load of Passenger Trains	12 tonnes
Axle Load of Freight Trains	22.5 tonnes
Speed Limit for Passenger Trains	70 km/h
Speed Limit for Freight Trains	70 km/h
Vehicle Velocity	120 km/h
Vehicle in Acceleration	35 km/h
Vehicle in Deceleration	30 km/h
Number of Daily Passenger Trains	10 Passenger Trains
Number of Freight Trains	23 Freight Trains
Gross Ton (Annually)	12.560.000 gtn



**CORRUGATION CATALOGUE**

**NETIRAIL-INFRA 636237**

**TYPE OF CORRUGATION:**



CORRUGATION	
Wavelength	100-300mm
Amplitude	30µm
Type of Corrugation	Medium Pitch
TRACK PARAMETERS	
Type of Rail	UIC 60 E
Rail Grade	900
Type of Sleepers	B70 Concrete
Type of Fastening System	Skl 14
Type of Rail Pad	RP 700
Curvature (Straight/Curve)	Curve
Lubrication Condition	Unavailable
Date of Renewal/ Reparation	2011

TRAFFIC	
Type of Traffic	Mixed Traffic
Single/ Double Traffic Direction	Double Traffic Condition
Axle Load of Passenger Trains	12 tonnes
Axle Load of Freight Trains	22.5 tonnes
Speed Limit for Passenger Trains	100 km/h
Speed Limit for Freight Trains	70 km/h
Vehicle Velocity	120 km/h
Vehicle in Acceleration	35 km/h
Vehicle in Deceleration	30 km/h
Number of Daily Passenger Trains	6 Passenger Trains
Number of Freight Trains	16 Freight Trains
Gross Ton (Annually)	8.600.000 gtn

**CORRUGATION CATALOGUE**

**NETIRAIL-INFRA 636237**

**TYPE OF CORRUGATION:**



CORRUGATION	
Wavelength	100-300mm
Amplitude	35µm
Type of Corrugation	Medium Pitch
TRACK PARAMETERS	
Type of Rail	UIC 60 E
Rail Grade	900
Type of Sleepers	B70 Concrete
Type of Fastening System	Skl 14
Type of Rail Pad	RP 700
Curvature (Straight/Curve)	Straight
Lubrication Condition	Unavaible
Date of Renewal/ Reparation	2012

TRAFFIC	
Type of Traffic	Mixed Traffic
Single/ Double Traffic Direction	Double Traffic Condition
Axle Load of Passenger Trains	12 tonnes
Axle Load of Freight Trains	22.5 tonnes
Speed Limit for Passenger Trains	100 km/h
Speed Limit for Freight Trains	70 km/h
Vehicle Velocity	120 km/h
Vehicle in Acceleration	35 km/h
Vehicle in Deceleration	30 km/h
Number of Daily Passenger Trains	6 Passenger Trains
Number of Freight Trains	22 Freight Trains
Gross Ton (Annually)	11.500.000 gtn

**CORRUGATION CATALOGUE**

**NETIRAIL-INFRA 636237**

**TYPE OF CORRUGATION:**



CORRUGATION	
Wavelength	30-100mm
Amplitude	10µm
Type of Corrugation	Short Pitch
TRACK PARAMETERS	
Type of Rail	UIC 60 E
Rail Grade	900
Type of Sleepers	B70 Concrete
Type of Fastening System	Skl 14
Type of Rail Pad	RP 700
Curvature (Straight/Curve)	Straight
Lubrication Condition	Unavailable
Date of Renewal/ Reparation	2011

TRAFFIC	
Type of Traffic	Mixed Traffic
Single/ Double Traffic Direction	Double Traffic Condition
Axle Load of Passenger Trains	12 tonnes
Axle Load of Freight Trains	22.5 tonnes
Speed Limit for Passenger Trains	100 km/h
Speed Limit for Freight Trains	70 km/h
Vehicle Velocity	120 km/h
Vehicle in Acceleration	35 km/h
Vehicle in Deceleration	30 km/h
Number of Daily Passenger Trains	8 Passenger Trains
Number of Freight Trains	14 Freight Trains
Gross Ton (Annually)	7.680.000 gtn